ΕΘΝΙΚΟ ΜΕΤΣΟΒΙΟ
ΠΟΛΥΤΕΧΝΕΙΟ
ΣΧΟΛΗ ΕΦΑΡΜΟΣΜΕΝΩΝ
ΜΑΘΗΜΑΤΙΚΩΝ
ΚΑΙ ΦΥΣΙΚΩΝ ΕΠΙΣΤΗΜΩΝ
ΣΧΟΛΗ ΜΗΧΑΝΟΛΟΓΩΝ
ΜΗΧΑΝΙΚΩΝ

ΕΚΕΦΕ «ΔΗΜΟΚΡΙΤΟΣ»
ΙΝΣΤΙΤΟΥΤΟ ΕΠΙΣΤΗΜΗΣ
ΥΛΙΚΩΝ
ΙΝΣΤΙΤΟΥΤΟ ΠΥΡΗΝΙΚΗΣ
ΦΥΣΙΚΗΣ

Διατμηματικό Πρόγραμμα Μεταπτυχιακών Σπουδών

«Φυσική και Τεχνολογικές Εφαρμογές»

Μέτρηση δεύτερης και ανώτερης τάξης συσχετίσεις Bose-Einstein πιονίων & μελέτη του φασματόμετρου μιονίων χρησιμοποιώντας τη διάσπαση $Z^0 \rightarrow \mu^+\mu^-$ σε συγκρούσεις πρωτονίων-πρωτονίων ενέργειας 7 TeV στο πείραμα ATLAS

ΜΕΤΑΠΤΥΧΙΑΚΗ ΔΙΠΛΩΜΑΤΙΚΗ ΕΡΓΑΣΙΑ

του Στέφανου Λεοντσίνη

Ερευνητικός Επιβλέπων:	Ακαδημαϊκός Επιβλέπων:
Θεόδωρος Αλεξόπουλος	Θεόδωρος Αλεξόπουλος

Αθήνα, Μάρτιος, 2012

**ΕΘΝΙΚΟ ΜΕΤΣΟΒΙΟ
ΠΟΛΥΤΕΧΝΕΙΟ
ΣΧΟΛΗ ΕΦΑΡΜΟΣΜΕΝΩΝ
ΜΑΘΗΜΑΤΙΚΩΝ
ΚΑΙ ΦΥΣΙΚΩΝ ΕΠΙΣΤΗΜΩΝ
ΣΧΟΛΗ ΜΗΧΑΝΟΛΟΓΩΝ
ΜΗΧΑΝΙΚΩΝ**

**ΕΚΕΦΕ «ΔΗΜΟΚΡΙΤΟΣ»
ΙΝΣΤΙΤΟΥΤΟ ΕΠΙΣΤΗΜΗΣ
ΥΛΙΚΩΝ
ΙΝΣΤΙΤΟΥΤΟ ΠΥΡΗΝΙΚΗΣ
ΦΥΣΙΚΗΣ**

Διατμηματικό Πρόγραμμα Μεταπτυχιακών Σπουδών

«Φυσική και Τεχνολογικές Εφαρμογές»

Μέτρηση δεύτερης και ανώτερης τάξης συσχετίσεις Bose-Einstein πιονίων & μελέτη του φασματόμετρου μιονίων χρησιμοποιώντας τη διάσπαση $Z^0 \rightarrow \mu^+\mu^-$ σε συγκρούσεις χπρωτονίων-πρωτονίων ενέργειας 7 TeV στο πείραμα ATLAS

ΜΕΤΑΠΤΥΧΙΑΚΗ ΔΙΠΛΩΜΑΤΙΚΗ ΕΡΓΑΣΙΑ

του Στέφανου Λεοντσίνη

Επιβλέπων: Θεόδωρος Αλεξόπουλος

Αθήνα, Μάρτιος, 2012

Ευχαριστίες

Για την εκπόνηση της παρούσης διπλωματικής εργασίας, θα ήθελα να εκφράσω τις ευχαριστίες μου στους παρακάτω:

- Τον επιβλέποντα καθηγητή μου κ. **Θεόδωρο Αλεξόπουλο**, τόσο για την ανάθεση της παρούσας πτυχιακής εργασίας όσο και για την συμπαράσταση και τις πολύτιμες συμβουλές του καθόλη τη διάρκεια της εκπόνησης, για τις γνώσεις που έχω αποκομήσει δουλεύοντας κοντά του και για τις ευκαιρίες που μου έχει δώσει.

- Τους γονείς μου, Γρηγόρη και Χριστίνα, τον αδερφό μου Σταμάτη για τις συμβουλές και την καθοδήγηση τους και για το ότι ήταν δίπλα μου όλες τις στιγμές. Δε θα μπορούσα να είχα ζητήσει καλύτερη οικογένεια.

- Τους συμφοιτητές και φίλους μου.

- Ιδαίτερα ευχαριστώ την κοπέλα μου, Αγγελική, που ήταν δίπλα μου συνέχεια. Στα καλά, αλλά περισσότερο στα άσχημα. Για την υπομονή της που ακόμη και στις (περιορισμένες) διακοπές μας, εγώ δουλευα και την ανοχή που δείχνει όταν δεν είμαι όπως θα έπρεπε να είμαι.

This page intentionally left blank

Περίληψη

Οι συσχετίσεις Bose-Einstein αποτελούν ένα απ' τα πιο χαρακτηριστικά αποτέλεσμα των ισχυρών αλληλεπιδράσεων. Στην παρούσα πτυχιακή εργασία μελετούνται συσχετίσεις Bose-Einstein δεύτερης και ανώτερης τάξης με δεδομένα απ' τον ανιχνευτή ATLAS. Αναλύονται $\sim 10^6$ $p-p$ αλληλεπιδράσεις ενέργειας στο κέντρο μάζας $\sqrt{s}=7$ TeV.

Από την κβαντομηχανική γνωρίζουμε πως αν εναλλάξουμε δύο από N μποζόνια, δεν αλλάζει η κυματοσυνάρτηση που περιγράφει την κατάσταση των μποζονίων. Αυτή η ιδιότητα της στατιστικής Bose-Einstein σημαίνει πως η κατάσταση Ψ έχει την ιδιότητα

$$\Psi(1,2,...,N)=\Psi(2,1,...,N)$$

η οποία οδηγεί στην γέννηση ομοίων μποζονίων.

Η πιθανότητα να παρατηρήσουμε δύο σωματίδια με ορμή $\boldsymbol{k}_1$ και $\boldsymbol{k}_2$ είναι

$$P(\boldsymbol{k}_1,\boldsymbol{k}_2)=\int|\psi_{1,2}|^2|\rho(\boldsymbol{r}_1)|^2|\rho(\boldsymbol{r}_2)|^2\mathrm{d}^3\boldsymbol{r_1}\mathrm{d}^3\boldsymbol{r_2}$$

όπου $\psi_{1,2}=\psi_{1,2}(\boldsymbol{k}_1\boldsymbol{k}_2,\boldsymbol{r}_1\boldsymbol{r}_2)$ η κυματοσυνάρτηση των δύο σωματιδίων.

Για δύο ταυτόσημα μποζόνια η συμμετρική $\psi_{1,2}$ έχει τη μορφή

$$\psi^s_{1,2}=\frac{1}{\sqrt{2}}\left[e^{i(\boldsymbol{k}_1\cdot\boldsymbol{r}_1+\boldsymbol{k}_2\cdot\boldsymbol{r}_2)}+e^{i(\boldsymbol{k}_1\cdot\boldsymbol{r}_2+\boldsymbol{k}_2\cdot\boldsymbol{r}_1)}\right]$$

καταλήγοντας στο

$$|\psi^s_{1,2}|^2=1+\cos\left[(\boldsymbol{k}_1-\boldsymbol{k}_2)(\boldsymbol{r}_1-\boldsymbol{r}_2)\right]=1+\cos\left[\Delta\boldsymbol{k}(\boldsymbol{r}_1-\boldsymbol{r}_2)\right]\ .$$

Χρησιμοποιώντας τα παραπάνω ορίζουμε τη συνάρτηση της συσχέτισης δεύτερης τάξης

$$C_2(\Delta\boldsymbol{k})=1+|\rho(\Delta\boldsymbol{k})|^2.$$

Στις περισσότερες Bose-Einstein αναλύσεις χρησιμοποιείται η αναλύωτη παράμετρος Q, που ορίζεται ως $Q^2=Q^2_2=-(q_1-q_2)^2=M^2_2-4m^2$, όπου m η μάζα των σωματιδίων. q_1, q_2 και M^2_2 είναι τα τετραδιανύσματα και η αναλύωτη μάζα στο τετράγωνο δύο ταυτόσημων μποζονίων μάζας μ. Υποθέτοντας επίσης ότι πηγή μπορεί να περιγραφεί από μια συμμετρική σφαιρική γκαουσιανή συνάρτηση

$$\rho(r)=\rho(0)e^{-r^2_0/2r^2_0}$$

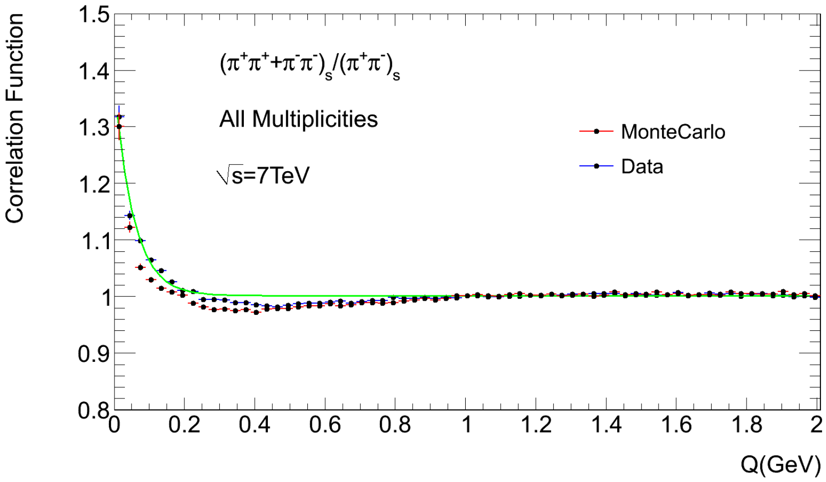

Figure 1: Λόγος ομόσημων/ετερόσημων ζεύγων πιονίων για δεδομένα και Monte Carlo.

τότε η συνάρτηση συσχέτισης Bose-Einstein παίρνει τη μορφή

$$C_2(Q) = 1 + e^{-r_G^2 Q^2}.$$

Για τη μέτρηση του φαινομένου Bose-Einstein χρησιμοποιήθηκαν δεδομένα απ' τον ανιχνευτή ATLAS. Αναλύθηκαν περίπου 10^6 γεγονότα τα οποία αντιστοιχούν σε 10^9 ζευγάρια ομόσημων πιονίων και 10^9 ζευγάρια ετερόσημων πιονίων. Ζητούμε όλα τα σωματίδια να έχουν τουλάχιστον 2 Pixel και 2 SCT hits με $p_T > 200$ MeV και $|\eta| < 2.5$. Επίσης πρέπει να καθαριστεί το sample από δευτερογενή πιόνια, όπως αυτά που προέρχονται απο σωματίδια όπως τα K_s^0 και Λ.

Οι κατανομές γίνονται fit με δύο συναρτήσεις. Την $1+\lambda e^{-rQ^2}$ και τη $\left(1+\lambda e^{-rQ^2}\right)/(1+\delta Q^2)$.

Η μέτρηση αυτή γίνεται και για 6 multiplicity bins. Χωρίζουμε το sample σε 6 υπο-samples ανάλογα με τη multiplicity του event. Τα αποτελέσματα φαίνονται στον παρακάτω πίνακα

Αποτελέσματα των fits σε δεδομένα ενέργειας 7 TeV

Multiplicity	λ	τ (fm)
2-9	0.862 ± 0.022	0.570 ± 0.014
10-14	0.566 ± 0.019	0.605 ± 0.018
15-19	0.455 ± 0.015	0.620 ± 0.019
20-29	0.382 ± 0.009	0.640 ± 0.014
30-39	0.298 ± 0.008	0.657 ± 0.011
40-79	0.247 ± 0.004	0.728 ± 0.010

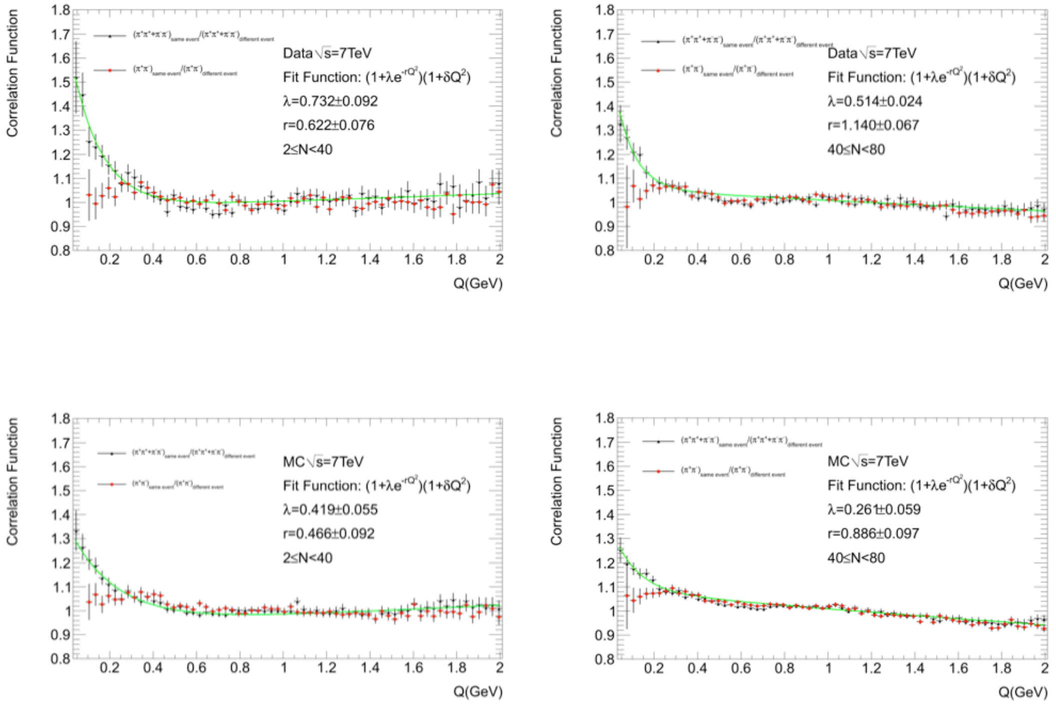

Figure 2: Συνάρτηση συσχέτισης για ομόσημα και ετερόσημα ζεύγη πιονίων για δύο διαφορετικά set αναλόγως της multiplicity τους ($2 \leq N < 40$ and $40 \leq N < 80$).

Στη συνέχεια έγινε και μελέτη τυχών συστηματικών που προσποιούταν το σήμα. Επαναλάβαμε την ίδια ανάλυση σε δίο διαφορετικά samples εκ των οποίων στο ένα (ομόσημα ζεύγη από το ίδιο γεγονός προς ομόσημα ζεύγη απο διαφορετικά γεγονότα) η κβαντομηχανική προβλέπει Bose-Einstein συσχετίσεις και σε ένα δεύτερο (ετερόσημα ζεύγη από το ίδιο γεγονός προς ετερόσημα ζεύγη απο διαφορετικά γεγονότα) για το οποίο δε προβλέπει.

Επιβεβαιώσαμε ότι δεν έχουμε συστηματικά όπως φαίνεται στο σχήμα.

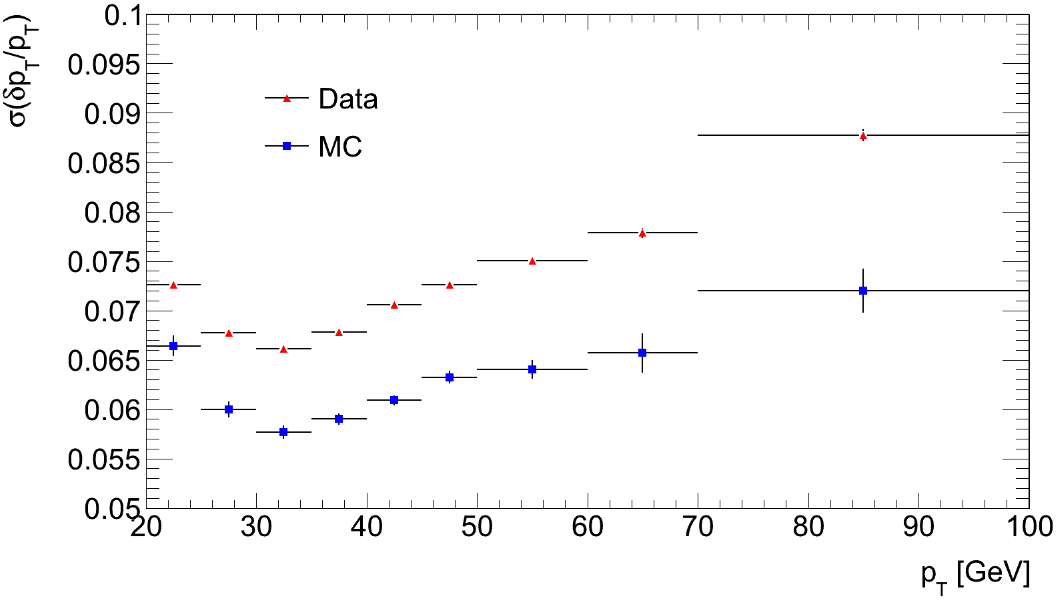

Figure 3: σ's τωνρ ως συνάρτηση της p_T

Στη συνέχεια χρησιμοποιούνται διασπάσεις του μποζονίου Z^0 σε $\mu^+\mu^-$ για τη μελέτη της απόδοσης του φασματόμετρου μιονίων.

Αφού κατασκευάσουμε ένα sample απο Z^0 τα οποία διασπούνται σε μιόνια, μελετούμε την ορμή που καταγράφετε στο εσωτερικό ανιχνευτή και το σπεκτρόμετρο μιονίων. Υπολογίζουμε την ποσότητα

$$\rho = \frac{p_{ID} - p_{MS}}{p_{ID}}$$

και τη χωρίζουμε σε 9 p_T bins. Στη συνέχεια εφαρμόζουμε ένα γκαουσιανό fit στις κατανομές αυτές και παίρνουμε το σ.

Καταλήγουμε στο resolution του μιονικού σπεκτρόμετρου όπως φαίνεται στην παρακάτω εικόνα.

Στο τελευταίο κομμάτι της εργασίας παρουσιάζονται δύο μέθοθοι για την ανακατασκευή στόχου με τη χρήση του ανιχνευτή MicroMeGas. Τα δεδομένα που αναλύθηκαν καταγράφηκαν κατά τη διάρκεια του Ιουλίου του 2011 στο H6 testbeam facility του CERN με δέσμες πιονίων.

Χρησιμοποιήθηκαν 3 ανιχνευτές (R14, R19M και R19G).

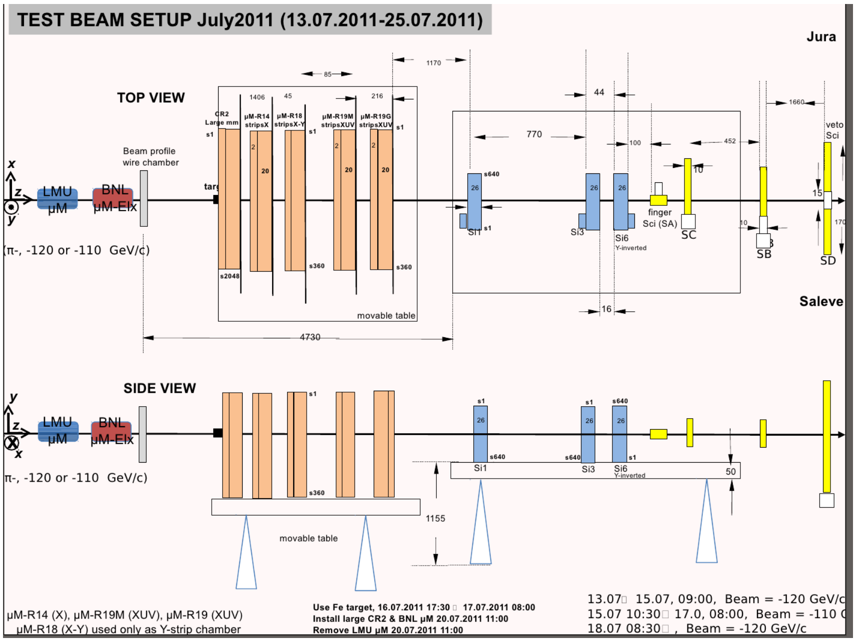

μM-R14 (X), μM-R19M (XUV), μM-R19 (XUV)
μM-R18 (X-Y) used only as Y-strip chamber

Use Fe target, 16.07.2011 17:30 17.07.2011 08:00
Install large CR2 & BNL μM 20.07.2011 11:00
Remove LMU μM 20.07.2011 11:00

13.07 15.07, 09:00, Beam = -120 GeV/c
15.07 10:30 17.0, 08:00, Beam = -110 G
18.07 08:30 , Beam = -120 GeV/c

Figure 4: Το setup των ανιχνευτών MicroMeGas R14, R19M and R19G.

Μέθοδος Α

Θεωρία

Χρησιμοποιούμε τις θέσεις των clusters των τριών MicroMegas για ανακατασκευάσουμε το σημείο γεγόνοτος. Για κάθε ζευγάρι από clusters (απαιτώντας τους clusters να είναι σε διαφορετικούς chambers), ανακαταστευάζουμε το σημείο τομής της ευθείας που ενώνει τα δύο clusters με τη γραμμή της δέσμης.

Το σημείο αυτό, x_v, δίνεται από τον τύπο:

$$x_v = \frac{x_j(m)z_i(n) - x_i(n)z_j(m)}{z_i(n) - z_j(m)} \tag{1}$$

όπου $(z_i(n), x_i(n))$, $(z_j(m), x_j(m))$ είναι οι συντεταγμένες του cluster n, στο επίπεδο i, και του cluster m στο επίπεδο j, αντίστοιχα. Λαμβάνοντας υπόψιν τη διακριτική

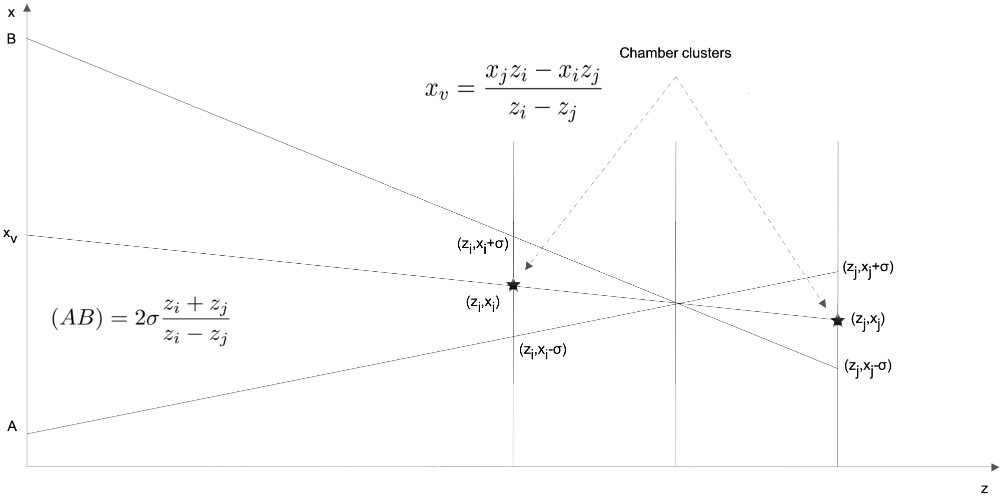

Figure 5: Δύο clusters σε δύο chambers και ο ορισμός των z_v και (AB).

ικανότητα του chamber resolution για τα hits αυτα, ένα smearing (AB) του x_v μπορεί να οριστεί ως:

$$(AB) = 2\sigma \frac{z_i(n) + z_j(m)}{|z_i(n) - z_j(m)|} \tag{2}$$

όπουσ είναι η διακριτική ικανότητα του cluster. Μια Lorentzian $L_{i,j}(n,m)$ κατασκευάζεται για τα δύο αυτά clusters

$$L_{i,j}(n,m) = \frac{1}{(x - x_v)^2 + (AB)^2/4} \tag{3}$$

όπου z_v και (AB) ορίζονται όπως παραπάνω. Η διαδικασία αυτή επαναλαμβάνεται για κάθε ζεύγος από clusters που βρίσκονται σε διαφορετικούς chambers. Αθροίζοντας όλες αυτές τις συνεισφορές , $L_{i,j}(n,m)$, για όλους τους πιθανούς clusters, ορίζουμε τη συνάρτηση $G(x)$ όπου περιγράφει τη πιαθνότητα του vertex point:

$$G(x) = \sum_{i}^{3} \sum_{j}^{3} \sum_{n}^{N_i} \sum_{m}^{N_j} L_{i,j}(n,m) \tag{4}$$

όπου N_i και N_j είναι οι αριθμοί των clusters στους chambers ($i = 1, \ldots, 3$), ($j = 1, \ldots, 3$), αντίστοιχα. Το μέγιστο της συνάρτησης $G(x)$ ορίζει το vertex του γενονότος event x_g. Η εικόνα **??** δείχνει την ανακατασκευή του event vertex για γεγονότα με φορτισμένα σωματίδια.

Αφού βρεθεί το x_v χρησιμοποιούμε την ίδια μέθοδο για να βρούμε το z_v.

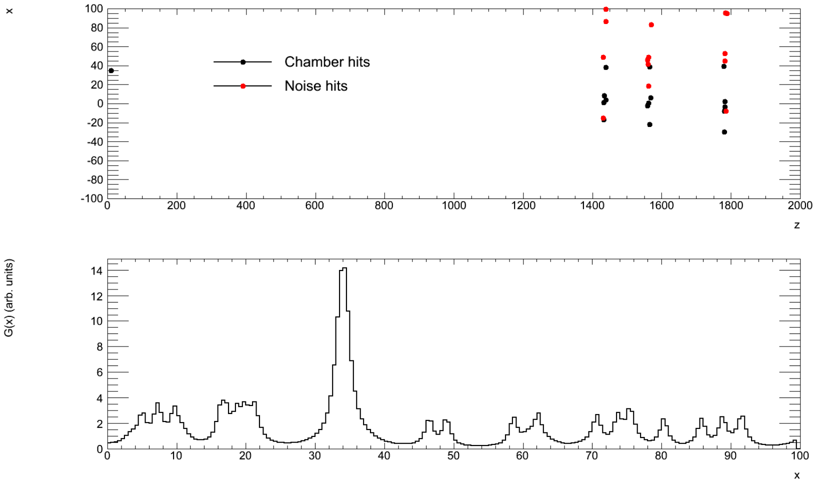

Figure 6: X-chamber σημεία χρησιμοποιούνται για την ανακατασκευή του event vertex ενός τυπικού γεγονότος με πολλά φορτισμένα σωματίδια, χρησιμοποιώντας τη μέθοδο A.

Αποτελέσματα

Monte Carlo

Η ανακατασκευή του vertex point, x_g, μελετήθηκε χρησιμοποιώντας Monte Carlo μεθόδους. Σ'αυτό το Monte Carlo , παράγουμε ομοιόμορφα έναν αριθμό από σωματίδια που προέρχεται απο ένα κοινό vertex point, x_{gen}. Κάθε σωματίδιο οδηγείται στους ανιχνευτές για να προσομοιωθούν οι clusters. Το vertex, x_{rec} ανακατασκευάζετε από τους προσομοιωμένους clusters χρησιμοποιώντας την παραπάνω μέθοδο. Φαίνεται ότι η μέθοδος αυτή ανακατασκευάζει το vertex point, x_g.

Εφαρμογή σε δεδομένα

x-άξονας

Χρησιμοποιούμε την μέθοδο οπυ περιγράφηκε παραπάνω σε 4 διαφορετικά set δεδομένων. Τρία sets που περιλαμβάνουν γεγονότα με το στόχο μεταξύ του σωλήνα της δέσμης και των ανιχνευτών (σε αποστάσεις 1.43m, 1m και 0.5m) και ένα set δεδομένων που περιλαμβάνουν δεδομένα που καταγράφηκαν χωρίς στόχο.

Εφαρμόζοντας τη μέθοδο στα γεγονότα χωρίς στόχο βλέπουμε το προφίλ της δέσμης όπως φαίνεται στην εικόνα **??**.

Εφαρμόζοντας τη μέθοδο αυτή σε δεδομένα που καταγράφηκαν με στόχο, το προφίλ

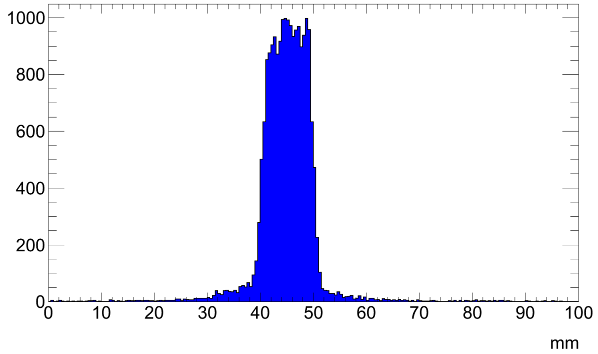

Figure 7: Το προφίλ της δέσμης.

της δέσμης γίνεται φαρδύτερο, πράγμα που αναμενόταν καθώς τα σωματίδια σκεδάζονται στο στόχο.

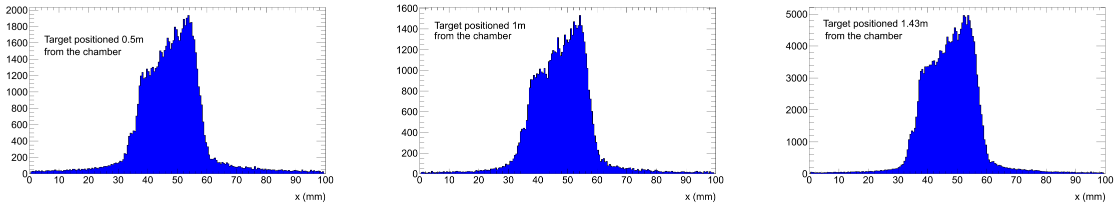

(a) Ο στόχος τοποθετημένος 0.5m απ' τους chambers.

(b) Ο στόχος τοποθετημένος 1.0m απ' τουςchambers.

(c) Ο στόχος τοποθετημένος 1.43m απ' τους chambers.

Figure 8: Το προφίλ της δέσμης για τρία set γεγονότων, με το στόχο τοποθετημένο μεταξύ των chambers και της δέσμης σε τρεις διαφορετικές αποστάσεις.

z-άξονας

Χρησιμοποιώντας την ίδια μέθοδο, έχοντας βρει το x_v προσπαθούμε να εντοπίσουμε το z_v. Εφαρμόζοντας τη μέθοδο αυτή στα δεδομένα που έχουν καταγραφεί χωρίς στόχο περιμένουμε να δούμε μια επίπεδη κατανομή, όπως φαίνεται και στην εικόνα **??**.

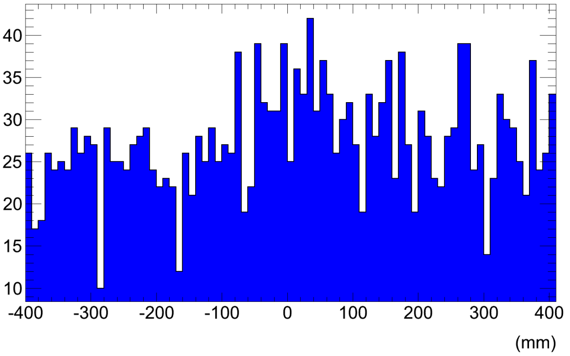

Figure 9: Επίπεδη κατανομή του z_v είναι αναμενόμενη, καθώς δεν υπάρχει ο στόχος μεταζύ της δέσμης και των chambers.

Αναλύοντας τα δεδομένα με το στόχο μεταξύ της δέσμης και των chambers παρατηρούμε ένα πλεόνασμα γεγονότων, το οποίο υποδεικνύει την ύπαρξη του στόχου. Αυτό φαίνεται στις κάτωθι εικόνες.

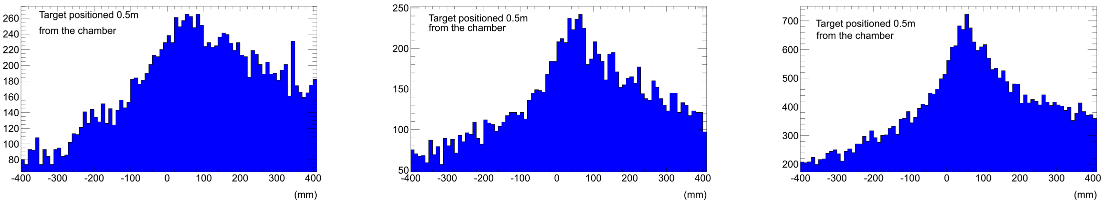

(a) Ο στόχος βρίσκεται 0.5m απ' τους chambers.

(b) Ο στόχος βρίσκεται 1.0m απ' τους chambers.

(c) Ο στόχος βρίσκεται 1.43m απ' τους chambers.

Figure 10: Μπορούμε να παρατηρήσουμε ένα πλεόνασμα γεγονότων στον z-άξονα, ένδειξη της ύπαρξης του στόχου μεταξύ της δέσμης και των chambers.

Μέθοδος B

Θεωρία

Χρησιμοποιώντας μια μέθοδο, παρόμοια με την A, για δύο ζεύγη από clusters (απαιτώντας οι clusters για κάθε ζεύγος να βρίσκεται σε διαφορετικούς chambers) κατασκευάζουμε μια δυδιάστατη γκαουσιανή στο σημείο όπου οι τροχιές απ' το κάθε ζεύγος των clusters σηναντούνται στο $x - z$ επίπεδο. Χρησιμοποιώντας τη μέθοδο αυτή μπορούμε να βρούμε τη θέση των x_v και z_v.

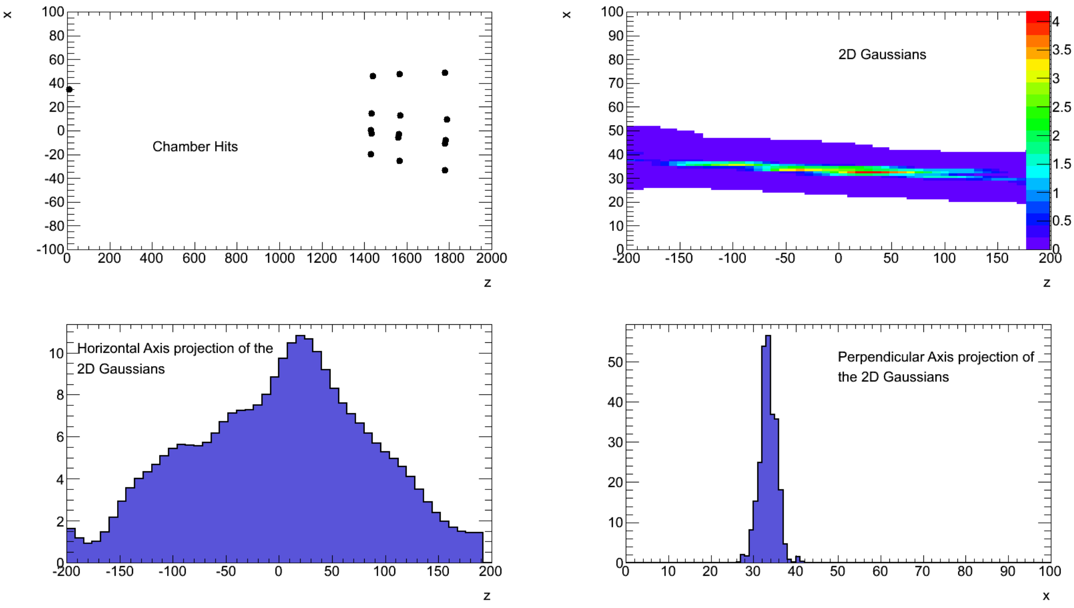

Figure 11: Τα σημεία X-chamber χρησιμοποιούνται για να κατασκευάσουμε το event vertex ενός τυπικού γεγονότος με τη χρήση της μεθόδου B

Αποτελέσματα

Monte Carlo

Κατασκευάσαμε μια προσομοίωση Monte Carlo, με ις ίδιες συνθήκες όπως και στην προηγούμενη μέθοδο.

Από τη δυδιάστατη γκαουσιανή παίρνουμε τις προβολές στον οριζόντιο και τον κατακόρυφο άξονα. Για τα set δεδομένων χωρίς στόχο περιμένουμε μια επίπεδη κατανομή στο z ενώ στο x περιμένουμε να δούμε το προφίλ της δέσμης.

Εφαρμόζοντας τη μέθοδο σε set δεδομένων με το στόχο τοποθετημένο μεταξύ των ανιχνευτών και της δέσμης πέρνουμε ένα φαρδύτερο προφίλ δέσμης και ένα πλεόνασμα γεγονότων σε ένα σημείο στον z άξονα, ένδειξη της ύπαρξης του στόχου.

x-άξονας

Εφαρμόζοντας τη μέθοδο σε ένα set γεγονότων χωρίς στόχο, παίρνουμε το προφίλ της δέσμης, όπως φαίνεται στην εικόνα **??**.

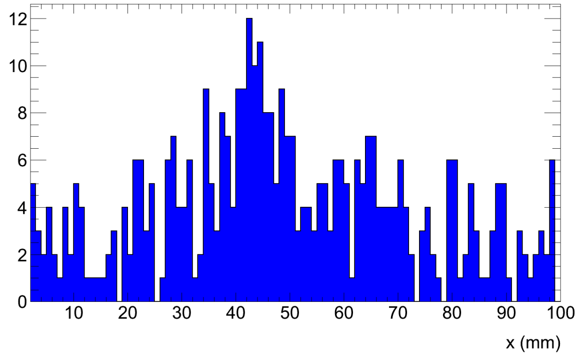

Figure 12: Το προφίλ της δέσμης.

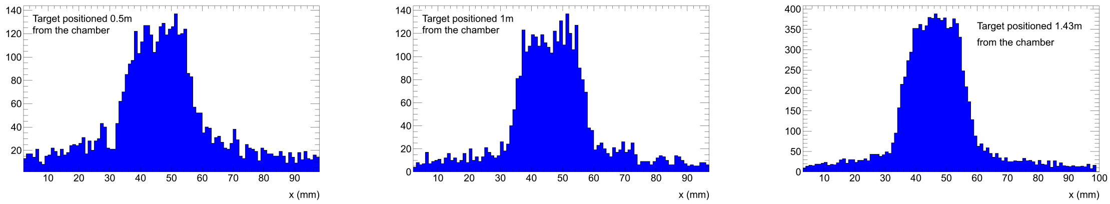

(a) Στόχος τοποθετημένος 0.5m $\alpha\pi$' τους chambers.

(b) Στόχος τοποθετημένος 1.0m $\alpha\pi$' τους chambers.

(c) Στόχος τοποθετημένος 1.43m $\alpha\pi$' τους chambers.

Figure 13: Το προφίλ της δέσμης για τρία set δεδομένων, έχοντας τοποθετήσει το στόχο μεταξύ της δέσμης και των ανιχνευτών σε τρεις διαφορετικές αποστάσεις.

z-άξονας

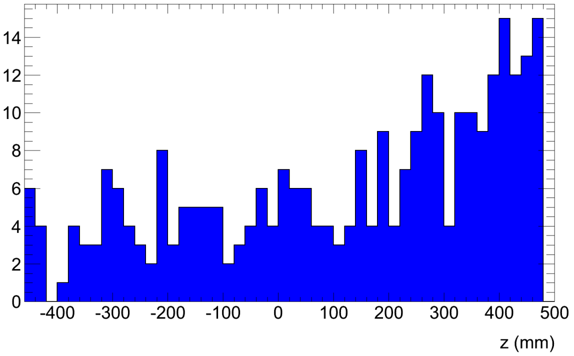

Figure 14: Επίπεδη κατανομή για το z_v είναι αναμενόμενη, καθώς δεν υπάρχει ο στόχος μεταξύ της δέσμης και των ανιχνευτών.

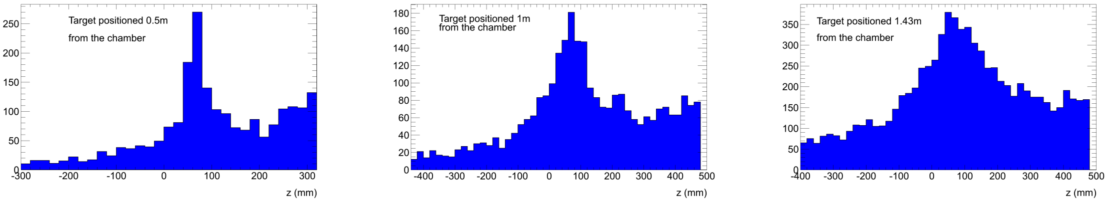

(a) Στόχος τοποθετημένος 0.5m απ' τους chambers.

(b) Στόχος τοποθετημένος 1.0m απ' τους chambers.

(c) Στόχος τοποθετημένος 1.43m απ' τους chambers.

Figure 15: Ένα πλεόνασμα γεγονότων αρχίζει να φαίνεται στον z-άξονα, ένδειξη ότι υπάρχει ένας στόχος τοποθετημένος μεταξύ της δέσμης και των ανιχνευτών.

Abstract

Bose-Einstein correlations constitute one of the most important and characteristic effects of strong interactions. In the present thesis we study two and three-pion Bose-Einstein correlations with data collected with the ATLAS detector. We analyze $\sim 10^6\ p-p$ interactions with at center of mass energy $\sqrt{s} = 7$ TeV.

The performance of the muon spectrometer it is also studied using the decay of $Z^0 \rightarrow \mu^+\mu^-$.

Finaly the reconstruction of a target using cluster positions on three MicroMeGas detectors.

This page intentionally left blank

Contents

Chapter 1

Theory

This chapter briefly reports the theoretical framework underlying the Bose-Einstein correlations (BEC).

1.1 Hanbury-Brown and Twiss Effect

The main idea of the "second-order interference", or Bose-Einstein correlation was first suggested in radioastronomy by R. Hanbury-Brown and R. Twiss in 1954 as a method of measuring the radii of distant stars. The Bose-Einstein phenomenon is caused by the ambiguity in the path of two identical boson particles (photons) considered:

- The direct amplitude due to the particle produced by source $S_1(S_2)$ hitting detector $D_1(D_2)$, respectively and,
- The exchange amplitude due to the particle produced by source $S_1(S_2)$ hitting detector $D_2(D_1)$, respectively.

The above two amplitudes overlap, and the probability of detecting a coincidence between the signals in D_1 and D_2 contains an interference term which depends on the dimensions of the source. This can be seen as follows:

Consider two points S_1 and S_2 on a source as shown in figure 1.1, each of which emits an infinitely long train of monochromatic photons with momenta $|\boldsymbol{p_1}| = |\boldsymbol{p_2}| = k$ and two detectors, D_1 and D_2 , measuring the intensity of the photons at distant points. The total amplitude A of this experiment can be written as a sum of the two above described amplitudes, (direct and exchange amplitude):

$$A \sim e^{ika_1} e^{ikb_1} + e^{ika_2} e^{ikb_2}, \tag{1.1}$$

where k is the momentum of the monochromatic photons, and a_2, a_2, b_1, and b_2 are the lengths of the four possible paths: $a_1 = |\boldsymbol{r_1} - \boldsymbol{x_1}|$, $a_2 = |\boldsymbol{r_2} - \boldsymbol{x_1}|$, $b_1 = |\boldsymbol{r_2} - \boldsymbol{x_2}|$ and $b_2 = |\boldsymbol{r_1} - \boldsymbol{x_2}|$. After some algebra the probability of observing the two photons is given by:

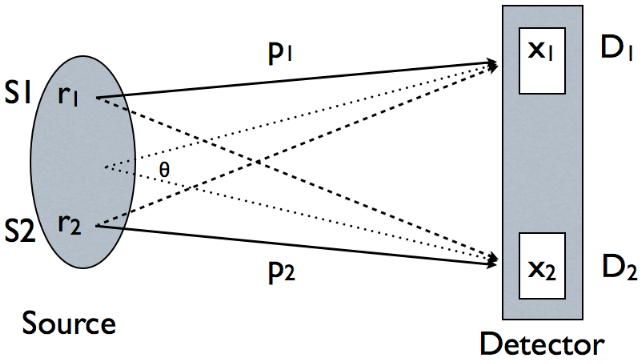

Figure 1.1: Two pions emitted from a pion source.

$$|A|^2 \sim 1 + \cos(kR\theta), \tag{1.2}$$

where R is the separation distance between the two source points $\boldsymbol{r_1}$, $\boldsymbol{r_2}$ and θ is the angular separation of the two detector points $\boldsymbol{x_1}$ and $\boldsymbol{x_2}$. A measurement of this probability or correlation function, $|A|^2$, as a function of the angular separation, θ, will be maximum at:

$$\frac{kR\theta}{2\pi} = 0, 1, 2, ..., n \tag{1.3}$$

Thus, by measuring the the angular separation, θ, of the two detector points $\boldsymbol{x_1}$ and $\boldsymbol{x_2}$ an estimation can be made of the separation distance between the two source points $\boldsymbol{r_1}$, and $\boldsymbol{r_2}$, as shown in Figure 1.1.

The extension of the above phenomenon to high energy physics was confirmed by Goldhaber. This first experimental evidence for Bose-Einstein correlation in particle physics goes back to 1960, when an enhancement at small angles in like-sign pion pairs was observed in $p\bar{p}$ annihilation at 1.05 GeV/c in a hydrogen bubble chamber. No similar effect was found in unlike-sign pairs. This enhancement was in contradiction with the statistical model, which could not predict this correlation in the opening angle of a pion pair. The reactions studied were of the form:

$$\bar{p} + p \rightarrow n^+\pi^+ + n^-\pi^- + n^0\pi^0, \tag{1.4}$$

where n^+, n^- and n^0 are the number of produced positive, negative and neutral pions, respectively.

In order to explain the above observed result, Goldhaber had to symmetrize the wave function that characterized the production of the n-pion state.

In the Fermi statistical model, the wave function of an $n-$pion state can be expressed as:

$$\Psi_n \sim e^{i\sum_{i=1}^{n}\boldsymbol{p_i}\cdot\boldsymbol{r_i}} \tag{1.5}$$

where $\boldsymbol{p_i}$ is the momentum vector of the $i-$th particle. The probability of observing the $n-$pion state created in an interaction region Ω is given by:

$$P_n \sim \int_{\Omega} |\Psi_n|^2 \mathrm{d}\boldsymbol{r_1}...\mathrm{d}\boldsymbol{r_n} \tag{1.6}$$

The only modification required by Goldhaber in order to explain the observed angle of the like sign pion pair was the explicit symmetrization of the wave function:

$$\Psi_n \sim \sum_{\sigma} e^{i\sum_{i=1}^{n}\boldsymbol{p}_{\sigma(i)}\cdot\boldsymbol{r_i}} \tag{1.7}$$

where $\sigma(i)$ is the i-th element of the permutation σ on n objects.

Many people followed Goldhaber in studying the correlation of the opening angle pion pairs.

An enhancement in the production of pairs of like charge and similar momentum has been observed in a variety of experiments including hadronic reactions, heavy-ion collisions, e^+e^- interactions , and μ-hadron collisions. As the energy of the interaction increased, more complicated dynamics created limitations on the direct application of the Goldhaber results. The difficulty was created by the inability to calculate the probability P_n. For the case of the two-pion state, Kopylov and Cocconi derived probability P_2. They used the fundamental work of R. Hanbury-Brown and R. Twiss as a guide in their work. The derivation of the probability function is given in the next section.

1.2 Bose-Einstein Correlations

1.2.1 The Bose-Einstein Correlation of Two Hadrons

As it is well known in quantum mechanics the interchange of two out of N indistinguishable bosons does not change the wave function describing this multi-boson state. This feature of the Bose-Einstein statistics means that the state Ψ has the property that

$$\Psi(1, 2, ..., N) = \Psi(2, 1, ..., N)$$

which leads to an interference term in $|\Psi|^2$ that enhances near in time-phase space the production of indistinguishable bosons. Let us first consider a source of discrete emission points, ρ_i, each characterized by a probability amplitude $F_i(\boldsymbol{r})$ in the 3-vector $\boldsymbol{r}_i$ phsase space

$$F_i(\boldsymbol{r}) = \rho_i \delta^3(\boldsymbol{r} - \boldsymbol{r}_i)$$

Next we introduce the central assumption pertaining to the BEC effect namely, the chaotic or the total incoherence limit, which corresponds to the situation where the phases of the production amplitudes wildly fluctuate in every point of space. In this limit all the phases can be set to zero. If $\psi_{\boldsymbol{k}(\boldsymbol{r})}$ is the wave function of the emitted particle, then the total probability $P(\boldsymbol{k})$ to observe the emission of one particle with a 3-momentum vector $\boldsymbol{k}$ is given by summing up the contributions from all the i points, that is

$$P(\boldsymbol{k}) = \sum_i |\rho_i \psi(\boldsymbol{r}_i)|^2 \ .$$

For simplicity we will further use plane wave functions $\psi_{\boldsymbol{k}} \propto e^{i(\boldsymbol{k}\cdot\boldsymbol{r}+\phi)}$ where in the incoherent case we can set $\phi = 0$. Next we replace the sum by an integral so that

$$P(\boldsymbol{k}) = \int |\rho(\boldsymbol{r})|^2 \mathrm{d}^3\boldsymbol{r}$$

The probability to observe two particles with momenta $\boldsymbol{k}_1$ and $\boldsymbol{k}_2$ is

$$P(\boldsymbol{k}_1, \boldsymbol{k}_2) = \int |\psi_{1,2}|^2 |\rho(\boldsymbol{r}_1)|^2 |\rho(\boldsymbol{r}_2)|^2 \mathrm{d}^3\boldsymbol{r_1} \mathrm{d}^3\boldsymbol{r_2}$$

where $\psi_{1,2} = \psi_{1,2}(\boldsymbol{k}_1, \boldsymbol{k}_2, \boldsymbol{r}_1, \boldsymbol{r}_2)$ is the two-particle wave function.

Taking incoherent plane waves, then for two identical bosons the symmetrised $\psi_{1,2}$ is of the form

$$\psi^s_{1,2} = \frac{1}{\sqrt{2}} \left[e^{i(\boldsymbol{k}_1\cdot\boldsymbol{r}_1 + \boldsymbol{k}_2\cdot\boldsymbol{r}_2)} + e^{i(\boldsymbol{k}_1\cdot\boldsymbol{r}_2 + \boldsymbol{k}_2\cdot\boldsymbol{r}_1)} \right]$$

so that

$$|\psi^s_{1,2}|^2 = 1 + \cos\left[(\boldsymbol{k}_1 - \boldsymbol{k}_2)(\boldsymbol{r}_1 - \boldsymbol{r}_2)\right] = 1 + \cos\left[\Delta\boldsymbol{k}(\boldsymbol{r}_1 - \boldsymbol{r}_2)\right] \ .$$

Using the above equations one can define a second order correlation function

$$C_2(\boldsymbol{k}_1, \boldsymbol{k}_2) \equiv \frac{P(\boldsymbol{k}_1, \boldsymbol{k}_2)}{P(\boldsymbol{k}_1)P(\boldsymbol{k}_2)} = 1 + \frac{\int \cos\left[\Delta\boldsymbol{k}(\boldsymbol{r}_1 - \boldsymbol{r}_2\right] |\rho(\boldsymbol{r}_1)|^2 |\rho(\boldsymbol{r}_2)|^2 \mathrm{d}^3\boldsymbol{r_1} \mathrm{d}^3\boldsymbol{r_2}}{P(\boldsymbol{k}_1)P(\boldsymbol{k}_2)} \ , \qquad (1.8)$$

where $\Delta\boldsymbol{k} = \boldsymbol{k}_1 - \boldsymbol{k}_2$. Assuming that the emitter extension $\rho\boldsymbol{r}$ is localised in space and time then it follows that when $\Delta\boldsymbol{k} = 0$ the last term of (1.8) can vary between the values 0 to 1. From (1.8) one obtains after the Fourier transformation

$$C_2(\Delta\boldsymbol{k}) = 1 + |\rho(\Delta\boldsymbol{k})|^2 \ .$$

In many of the two-boson one dimensional BEC analyses one uses the Lorentz invariant parameter Q, defined as $Q^2 = Q_2^2 = -(q_1 - q_2)^2 \equiv M_2^2 - 4m^2$, where m is the mass of the particles . Here $q_1,\ q_2$ and $M_2^2$are respectively the 4-momentum vectors and invariant mass squared of the two identical bosons of mass μ.

Thus one obtains

$$C_2(Q) = 1 + |\rho(Q)|^2$$

Assuming further that the source is described by a spherical symmetric Gaussian density distribution of emitting centres

$$\rho(r) = \rho(0)e^{-r^2/2r_0^2}$$

then the Bose-Einstein correlation function assumes the form

$$C_2(\Delta\boldsymbol{k}) = 1 + e^{-r_0^2\Delta\boldsymbol{k}^2}$$

In terms of the variable Q and the dimension r_G, introduced by Goldhaber et al., the correlation function in the completely chaotic limit is equal to

$$C_2(Q) = 1 + e^{-r_G^2Q^2} \tag{1.9}$$

In the completely coherent case it can be shown that $C_2(Q) = 1$. In order to accommodate those cases where the source is not completely chaotic one introduces a chaoticity parameter λ_2 which can vary between the value 0, corresponding to a complete coherent case, to the value 1 at the total chaotic limit. Thus (1.9) is transformed to the form

$$C_2(Q) = N\left(1 + \lambda_2 e^{-r_G^2Q^2}\right) \tag{1.10}$$

where N is added as a normalisation factor. Since the strength of the BEC effect depends also on the experimental data quality, like the purity of the identical boson sample, λ_2 is often also referred to as the BEC strength parameter. In the following, unless otherwise stated, we will deonote by r the dimension values obtained from BEC analyses which used the GGLP (Goldhaber, Goldhaber, Lee and Pais) parametrisation, that is $r \equiv r_G$.

1.2.2 Higher Order Bose-Einstein Correlations

A Bose-Einstein correlation enhancement is also expected to be present in identical boson systems of more than two particles when they emerge from the interaction within a small time- space region. In the search for these so called, higher order BEC enhancements, one has to differentiate between those produced from the lower BEC order(s) and those who are genuine correlations. The normalised over-all inclusive correlations of n identical bosons is given by

$$R_n = \frac{\rho_n(p_1, p_2, ..., p_n)}{\rho_1(p_1)\rho_1(p_2)...\rho_1(p_n)} = \sigma^{n-1}\frac{d^n\sigma}{dp_1dp_2...dp_n}\bigg/\left(\frac{d\sigma}{dp_1}\frac{d\sigma}{dp_2}\cdots\frac{d\sigma}{dp_n}\right) \tag{1.11}$$

where σ is the total boson production cross section, $\rho_1(p_i)$ and $d\sigma/dp_i$ are the single-boson density in momentum space and the inclusive cross section, respectively. Similarly $\rho_n(p_1, p_2, ..., p_n)$ and $d\sigma/(dp_1 dp_2 ... dp_n)$ are respectively the density of the n-boson system and its inclusive cross section. The product of the independent one-particle densities $\rho_1(p_1)\rho_1(p_2)...\rho_1(p_n)$ is referred to as the reference density distribution, or reference sample, to which the measured correlations are compared to. Specifically the inclusive two-boson density $\rho_2(p_1, p_2)$ can be written as

$$\rho_2(p_1, p_2) = \rho_1(p_1)\rho_1(p_2) + K_2(p_1, p_2)$$

where $\rho_1(p_1)\rho_1(p_2)$ represents the two independent boson momentum spectra and $K_2(p_1, p_2)$ desscribes the two-body correlations. In this simple case of two identical bosons the normalised density function R_2 defined by (1.11), already measures the genuine two-body correlations which here is referred to as the C_2 correlation funciton. Thus one has

$$C_2 \equiv R_2 = 1 + \widetilde{K}_2(p_1, p_2)$$

where $\widetilde{K}_2(p_1, p_2) = K_2(p_1, p_2)/[\rho_1(p_1)\rho_1(p_2)]$ is the normalised two-body correlation term which in the GGLP parametrisation is equal to $\lambda_2 e^{-Q_2^2 r_2^2}$.

The inclusive correlation of three identical bosons, $\rho_3(p_1, p_2, p_3)$, includes the three independent boson momentum spectra, the two-particle correlation K_2 and the genuine three-particle correlation K_3, namely

$$\rho_3(p_1, p_2, p_3) = \rho_1(p_1)\rho_1(p_2)\rho_1(p_3) + \sum_{(3)} \rho_1(p_i)K_2(p_j, p_k) + K_3(p_1, p_2, p_3)$$

where the summation is taken over all the three possible permutations. The normalised inclusive three-body density, is then given by

$$R_3 = \frac{\rho_3(p_1, p_2, p_3)}{\rho_1(p_1)\rho_1(p_2)\rho_1(p_3)} = 1 + R_{1,2} + \widetilde{K}_3(p_1, p_2, p_3)$$

Here

$$R_{1,2} = \frac{\sum_{(3)} \rho_1(p_i)K_2(p_j, p_k)}{\rho_1(p_1)\rho_1(p_2)\rho_1(p_3)}$$

and

$$\widetilde{K}_3(p_1, p_2, p_3) = \frac{K_3(p_1, p_2, p_3)}{\rho_1(p_1)\rho_1(p_2)\rho_1(p_3)}$$

represent the mixed three-boson system in which only two of them are correlated and the three- boson correlation. In analogy to C_2, one defines a correlation function C_3 which measures the genuine three-boson correlation, by subtracting from R_3 the term which contains the two-boson correlation contribution. Thus

$$C_3 \equiv R_3 - R_{1,2} = 1 + \widetilde{K}_3(p_1, p_2, p_3)$$

which depends only on the genuine three-boson correlation. For the study of the three-boson correlation one often uses the variable Q_3 which, analogous to the varialbe Q_2^2, is defined as

$$Q_3^2 = \sum_{(3)} q_{i,j}^2 = M_3^2 - 9\mu^2$$

where the summation is taken over all the three different i, j boson-pairs. Here M_3^2 is the invariant mass squared of the three-boson system and μ is the mass of the single boson. From the definition of this three-boson variable it is clear that as Q_3 approaches zero so do all the three related $q_{i,j}$ values which eventually reach the region where the two-boson BEC enhancements are observed. It has been shown that the genuine three-pion correlation function $C_3(Q_3)$ can be parametrised by the expression

$$C_3(Q_3) = 1 + 2\lambda_3 e^{-Q_3^2 r_3^2}$$

where λ_3 is the chaoticity parameter which may assume a value between zero and one.

1.3 Standard Model Physics

The Standard Model describes the behavior of matter and it's interactions. This theoretical framework managed to give a unified description of strong, electromagnetic and weak interactions but the gravity, describing the matter as point-like spin-1/2 fermions and the interactions as spin-1 gauge bosons.

The model is based on the gauge symmetry group

$$SU_C(3) \times SU_L(2) \times U_Y(1) \tag{1.12}$$

where the first factor describes the strong colour interactions, carried by 8 gluons, while $SU_L(2) \times U_Y(1)$ is the symmetry group of unified electro-weak interactions, carried by the photon and the Z^0 and $W^\pm$ bosons.

In gauge theories all the gauge bosons should be massless, but experimentally the weak $W^\pm$ and Z^0 bosons, have mass. The Standard Model solves this problem introducing a scalar particle, the Higgs boson, which couples to massive particles and gives them masses through a spontaneous symmetry breaking mechanism. To our experimental knowledge there are three families of fermions, each containing two quarks, a charged lepton and a neutrino. Fermion masses are also obtained by the Higgs mechanism through Yukawa couplings between the fermion and the Higgs.

The Standard Model has been extensively tested in the last decades at LEP and Tevatron and it turned out that it successfully explains most of the known phenomena in elementary particle physics. Nevertheless a number of open questions are still left which need for further studies to be done.

There is, for example, evidence that neutrinos have non-zero masses, which the SM does not allow. The measurement of the ordinary matter density in our universe gives a hint that physics even beyond the SM should exist. Astrophysics observations make it clear for example that either our understanding of gravity based on Einstein's theory of General Relativity is wrong, or that particles forming dark matter, which have so far escaped our detection, must exist, and the SM does not furnish any viable candidate. Moreover the observed matter-antimatter asymmetry is not explained in the SM framework.

There also are theoretical motivations for thinking that the SM needs to be extended. One such example is the hierarchy problem concerning the quadratically divergent fermion loop corrections to the Higgs boson mass. New physics is required to happen at the TeV scale to constrain the Higgs mass in the area of a few hundred GeV and thus make the SM consistent with recent W and top mass measurements. The unification of the gauge couplings is something which is aimed but it does not happen in the SM. In addition the unification of gravity with the other forces is still missing.

The Large Hadron Collider has been built, with its four experiments, ATLAS, CMS, LHCb and ALICE, to answer this kind of questions. The composite nature of the proton-proton collisions, despite of the difficult experimental environment which generates, opens a wide range of exploration possibilities, from the precise measurements of Standard Model parameters to the search for new physics phenomena up to the TeV scale.

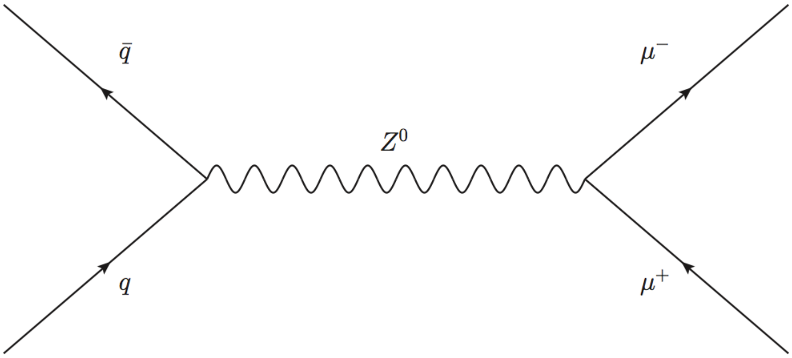

Figure 1.2: Feynman graph for the $Z^0 \to \mu^+\mu^-$ process

Nevertheless, all these searches should be preceded by the measurement of the well known Standard Model processes. These can be used as standard candles both for the detectors understanding and performance assessment, and the theoretical predictions tuning at a new unexplored energy. Particularly suitable to this extent is the study of the production of the $W^\pm$ and Z^0 bosons, because the theoretical predictions have a small uncertainty. They have also been measured at LEP and at Tevatron with big precision.

1.3.1 $W^\pm$ and Z^0 Boson Physics: the Drell-Yan Process

The Drell-Yan process is likely to be the standard candle which is both theoretically calculable and experimentally measurable with highest accuracy at hadron colliders, in particular at the LHC. It consists in the production of a neutral or charged lepton pair, $l\bar{l}$ or $l\bar{\nu}$, in the collision of two initial hadrons H_1 and H_2:

$$H_1(p_1) + H_2(p_2) \to l(k_1) + \bar{l}(k_2) + X(q) \tag{1.13}$$

$$H_1(p_1) + H_2(p_2) \to l(k_1) + \bar{\nu}(k_2) + X(q) \tag{1.14}$$

where p_i are the momenta of the incoming partons, k_i are the momenta of the outgoing partons and X is the entire set of other hadronic objects produced in the event. In the parton model, the generic differential cross-section for the process is

$$d\sigma(p_1,p_2) = \sum_{i,j} \int_\tau^1 dx_1 \int_{\tau/x_1}^1 dx_2 f_i^{(1)}(x_1) f_j^{(2)}(x_2) d\hat{\sigma}_{ij}(x_1p_1, x_2p_2), \tag{1.15}$$

where $f_i^{(H)}(x)$ are the parton density functions of parton i in the initial hadron H, carrying a momentum fraction x, and $\tau = M^2/s$. $d\hat{\sigma}_{ij}(\hat{p}_1, \hat{p}_2)$ is the parton-level cross-section, which depends on the initial parton momenta $\hat{p}_1, \hat{p}_2$ and on the parton species i, j. The sum extends to all quarks and gluons in the initial hadrons.

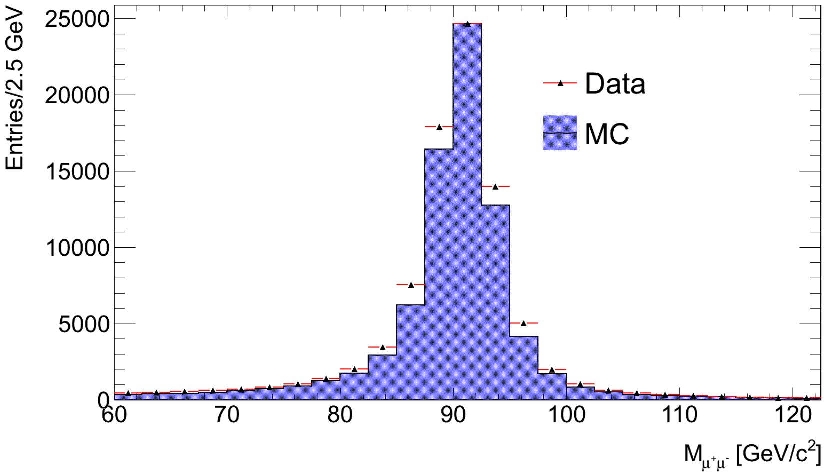

Figure 1.3: $\mu^+\mu^-$ invariant mass using ATLAS data

At leading order in both electroweak and QCD the partonic process consists of a quark and an antiquark annihilating into a virtual vector boson γ, Z^0 or $W^\pm$, which subsequently decays into the lepton pair. At this order all the available partonic center-of-mass energy $\sqrt{\hat{s}}$,

$$\hat{s} = x_1 x_2 s, \qquad s = (p_1 + p_2)^2\,, \tag{1.16}$$

goes into the lepton pair invariant mass M,

$$M^2 = (k_1 + k_2)^2\,. \tag{1.17}$$

When QCD correction on the initial partons are considered, real emission of gluons and quarks must be taken into account, in order to remove infrared divergences coming from virtual corrections. These emissions can be soft (hence undetectable, making this process indistinguishable from the process with no emission) or hard (producing jets). In this case the available partonic center-of-mass energy is no longer equal to the final state mass.

The current QCD theoretical accuracy for this process is NNLO, both for the integrated cross-section and the rapidity-distributions.

A large number of events collected at the LHC, combined with a very precise theoretical determination of the process, can be a very useful test of perturbative QCD. Moreover, the high LHC energy will allow for detailed measurements at a previously unexplored kinematic domain of low parton momentum fraction at a high energy scale, significantly improving the precision on the determination of the PDFs.

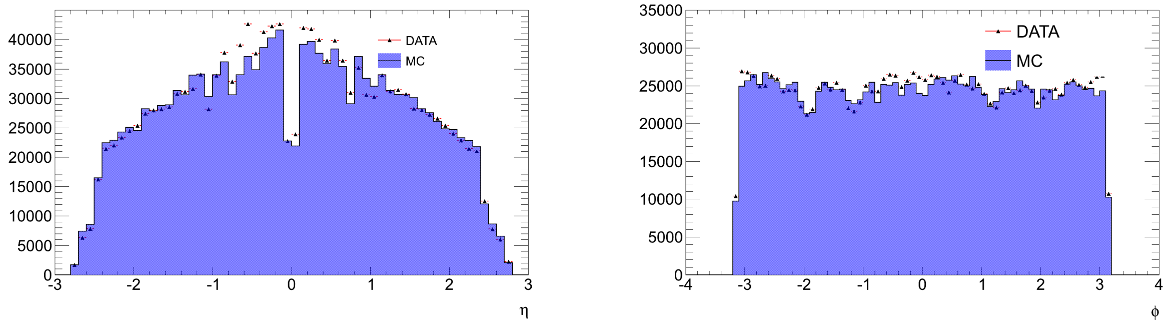

(a) η distribution of the muons coming from the Z^0.

(b) ϕ distribution of the muons coming from the Z^0.

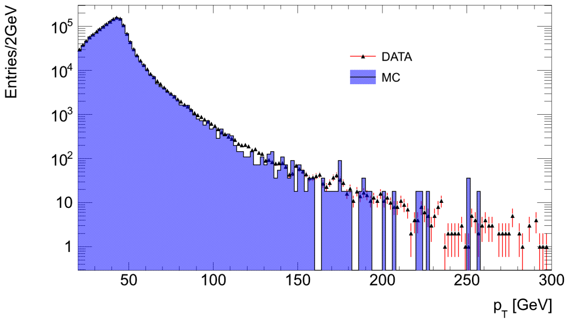

(c) p_T distribution of the muons coming from the Z^0.

Figure 1.4: Distributions of the muons coming from the Z^0.

This page intentionally left blank

Chapter 2

LHC Accelerator and the ATLAS Detector

This chapter will give an overview on the LHC and a description of the ATLAS detector.

2.1 The Accelerator

The LHC consists of two rings with counter-rotating beams. The LHC is constructed in the 26.7 km circular tunnel of the LEP at CERN in Geneva, Switzerland. In the LHC bunches of protons are injected from the Super Proton Synchrotron (SPS) with an energy of 450 MeV and then accelerated using a system of eight superconducting cavities per beam. The proton energy is determined by the given curvature of the LHC tunnel and the maximum field of the dipole magnets responsible for bending the beam.

Bending, steering and focusing of the proton beam is controlled with over 9000 magnets. The 1232 dipole magnets responsible for the bending are supported by multipole corrector magnets (sextupoles, octupoles and decapoles) to stabilise the beam. The 392 main quadrupole magnets and the associated corrector magnets (dipoles, sextupoles and octupoles) are responsible for the beam focus. The final focusing of the beams around the four interaction points is caused by dedicated high aperture triplet quadrupoles.

Along with the beam energy the second parameter crucial for the LHC is the luminosity, which in principle defines the number of collisions per time interval for a given cross section. A high luminosity can be reached by colliding beams with a high number of protons per beam on a small area with a high frequency. Luminosity can be expressed by the following term:

$$\mathcal{L} = \frac{N_b^2 n_b f_{rev}}{4\pi \sigma_x^* \sigma_y^*} F \ , \tag{2.1}$$

where N_b is the number of protons per bunch, n_b is the number of bunches per beam, f_{rev} is the revolution frequency and $\sigma^*_{x,y}$ the RMS of the transverse beam size at the interaction point in $x-$ and $y-$direction. Often the beam size is written as a product of the two beam

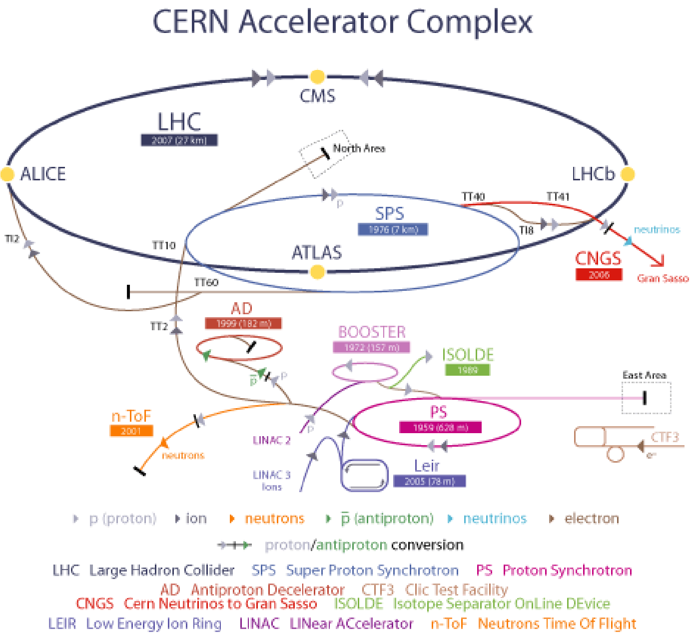

Figure 2.1: Schematic overview of the Large Hadron Collider.

parameters, the transverse beam emittance that corresponds to the phase space covered by the beam ϵ and the betatron function β^*. Due to the crossing angle at the interaction point Θ_c the luminosity is decreased by the geometric luminosity reduction factor F:

$$F = \left(1 + \left(\frac{\Theta_c \sigma_z}{2\sigma^*}\right)^2\right)^{-\frac{1}{2}} \tag{2.2}$$

where σ_z is the RMS of the bunch length in beam direction and σ^* the RMS of the transverse beam size.

2.2 The ATLAS Detector

The ATLAS detector is a general purpose detector. The main motivation might be the unraveling of the electroweak symmetry breaking and the discovery of the Higgs boson, but the collaboration cover a broad range of searches within the standard model and beyond (CP violation, supersymmetry, remnants of dark matter, etc.).

The detector layout consists of detector components arranged in layers concentrically around the collision point. The layer closest to the interaction point is the Inner Detector, dedicated to the measurement of charged particle tracks, allowing the reconstruction of the particles charge, momentum and production vertex. The next two layers are designed to measure the energy deposit of electrons and photons, the electromagnetic calorimeter,

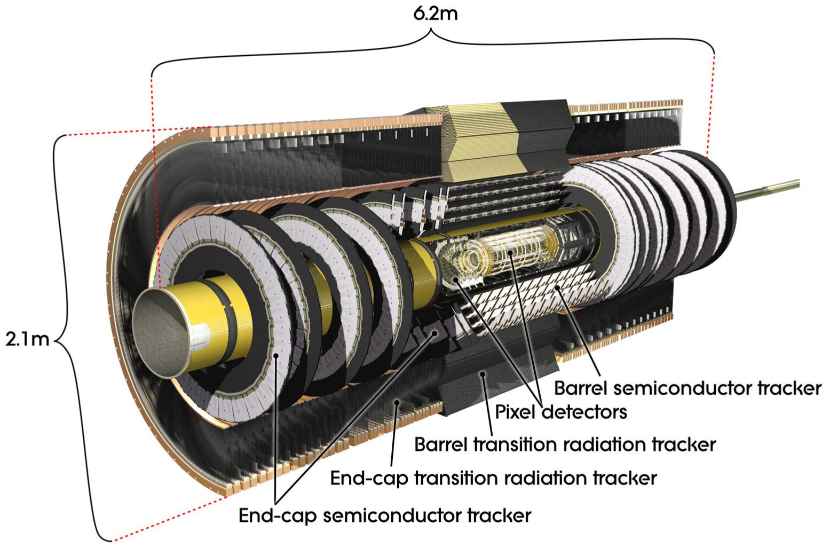

Figure 2.2: Schematic overview of the ATLAS Inner Detector.

and of hadrons in the hadronic calorimeter. The outermost layer is the muon spectrometer, which is responsible for the large size of of the ATLAS detector. In the muon spectrometer the muons momentum can be measured at high precision.

Inner Detector

The Inner Detector of the ATLAS experiment has three main detector parts. The three parts are separated in a barrel and two end-cap regions. In the barrel region, the innermost part closest to the collision point is a silicon pixel detector, with a total number of three layers of silicon pixel modules with radial distances between 50.5 mm and 122.5 mm. Following the same physical principle, a silicon microstrip detector (Semiconductor Tracker SCT) provides four additional layers at radii between 299 mm and 514 mm. The Transition Radiation Tracker (TRT) is the outermost layer of the Inner Detector, starting at radius 554 mm up to 1082 mm. Its dimension defines the total diameter of the Inner Detector of approximately 2.1 m.

In order to provide a good coverage in pseudo-rapidity, end-cap disks of the Pixel detector and SCT are designed to cover particle tracks up to a pseudo-rapidity of $|\eta| = 2.5$. The TRT end-cap can cover particles up to approximately $|\eta| = 2.0$. Including all of the supporting structure, the cylindrical envelope holding the Inner Detector in total has a length of 7.0 m.

The inner solenoidal magnet system surrounding the Inner Detector is creating an axial symmetric magnetic field of 2 T bending charged particles into the $R - \phi$ plane due to the Lorentz force. This allows the measurement of the particles transverse momenta down to a minimum of $p_T = 0.5$ GeV. Particles with a p_T lower than 0.5 GeV are bended

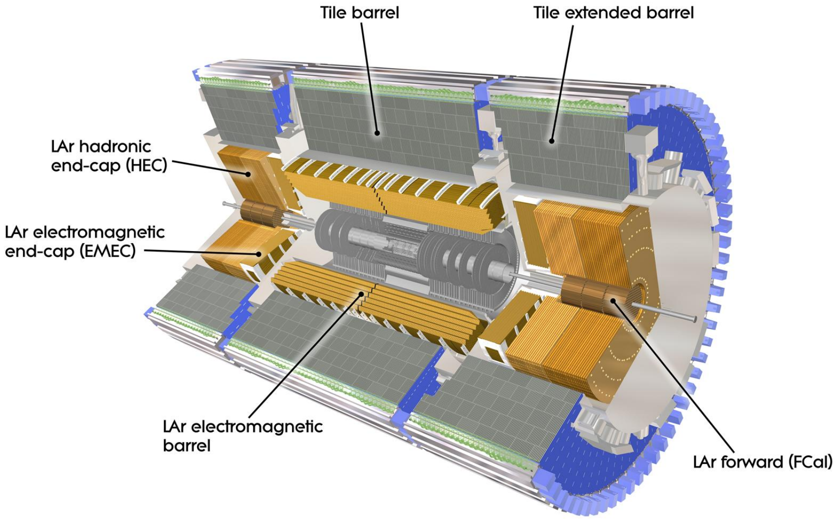

Figure 2.3: Schematic overview of the ATLAS calorimeter.

to very small radii, preventing the particles to leave the Inner Detector. Additional, at low momentum the efficiency is reduced due to large material effects.

Calorimeter

In general, the energy of all stable particles but muons and neutrinos can be measured in a calorimeter. A particle entering a calorimeter looses all its energy in a particle shower. The total particle energy is reconstructed by measuring ionization, scintillation light or Cherenkov radiation.

In the ATLAS detector the calorimetry system is divided into a number of sampling detectors dedicated to the measurement of the particles energies. In principle particles entering a calorimeter transfer their energy to the detector material, producing new particles by interactions with the detector material in the calorimeter. Typical interactions are e.g. the production of new photons due to bremsstrahlung or the creation of an electron positron pair due to the interaction of a photon with the coulomb field of an atom. These secondary new particles interact themselves with the calorimeter, creating new particles until the particles energy is too low to create new particles. Due to this cascade one particle entering the calorimeter leaves a shower of particles, each with low energy. By measuring the total energy of all particles created in this shower, the initial particles energy can be reconstructed.

One of the main requirements of the calorimeter is the hermeticity in order to measure missing transverse energy $E_{T,miss}$ at a good resolution. The ATLAS calorimeter fulfills this requirement with a coverage over the whole range of ϕ and up to a pseudo-rapidity of

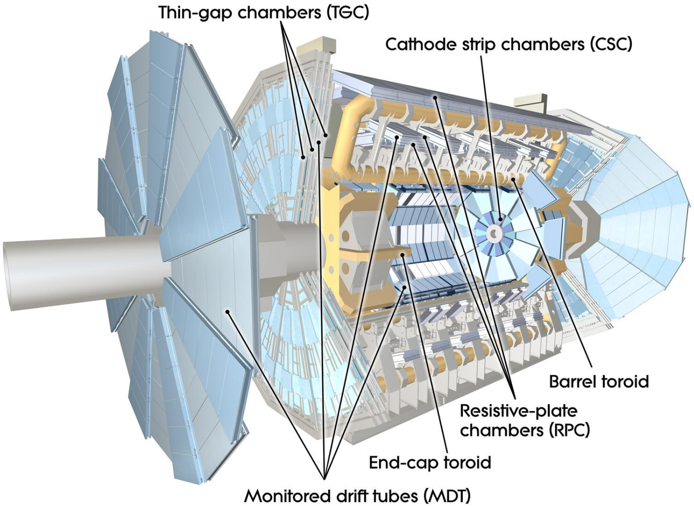

Figure 2.4: Schematic overview of the ATLAS muon spectrometer.

$|\eta| = 4.9$. Surrounding the Inner Detector and solenoidal magnetic system, the calorimeter itself is split into several parts, depending on the type of interactions particles undergo in the detector material and the position within the detector.

The separation due to the interaction allows the differentiation into two groups of particles. In the electromagnetic calorimeters electrons (positrons) and photons are detected, in the hadronic calorimeters particles interacting mainly via the strong force are measured. The electromagnetic calorimeter is required to provide a fine segmentation for a precise measurement of electrons and photons. As the hadronic calorimeter mainly aims at the reconstruction of jets and the measurement of missing energy, the granularity is more coarse.

In the barrel region the innermost part of the calorimetry system is the LAr electromagnetic barrel surrounded by the hadronic Tile barrel. In the end-cap region, a LAr electromagnetic end-cap (EMEC) is followed by a LAr hadronic end-cap (HEC). In addition, covering the region close to the beam pipe, the forward calorimeter FCal detects electromagnetically interacting particles at large pseudo-rapidity.

Muon System

Over a large area of pseudo-rapidity up to $|\eta| < 2.7$, the muon track coordinates are measured by monitored drift tubes (MDT). In the barrel region, the MDT chambers are aligned in three layers: the innermost layer surrounding the tile calorimeter, one layer between the barrel toroid BT and the outermost layer enclosing the BT.

In principle, the measurement of the muons momenta is a measurement of the particles trajectory at three spacepoints. While in the barrel region one layer of muon chambers is placed within the toroidal magnet system, in the end-caps the toroid is placed between the first and the second layer. Hence, the measurement principle differs in these two regions. In the case of the barrel region, the muons momentum is reconstructed from the measurement of the trajectories deviation of a straight line, the so called sagitta s, and the direct distance L between the two measurement points in the first and third layer. Taking into account the magnetic field B, the transverse momentum is calculated as

$$p_T = \frac{L^2 B}{8s} \tag{2.3}$$

In the case of the end-caps, the trajectory is bent between the first two layers of muon chambers, but a straight line between the second and the third layer. Hence, the reconstruction of the muons momentum depends on a point angle measurement.

The muon system is able to perform a stand-alone reconstruction of muons momentum at a resolution of 10% for tracks with a momentum of 1 TeV. It is capable to measure muon tracks with a momentum of a few GeV, also standalone.

Chapter 3

ROOT and the Athena Framework

3.1 ROOT

Root is a powerful data analysis framework developed for CERN, the international physics organization behind the Large Hadron Collider particle accelerator experiment in Switzerland that aims to find the theoretical Higgs Boson. Because of the massive amounts of data the LHC will generate in searching for the Higgs boson and new physics, CERN scientists required a new, more powerful framework to handle the analysis of the large datasets from the particle collision experiments the LHC is expected to carry out in the coming years.

Root is an object-oriented framework developed in C++, the language used by most of the LHC experiments, including the CMS (Central Muon Solenoid) project, in which the Purdue Physics Department is an active participant and contributor. An integral part of Root is CINT, its dynamic C++ interpreter which drives its computations and powerful programming capabilities. Because of its close relationship to C++ and its development for CERN as a data analysis framework that must be easily and readily distributed to thousands of scientists worldwide for physics analyses for the output of the LHC, Root is run as a Unix program, which may be unconventional for statisticians who are more familiar with applications like SAS and R. However, the advantage is that much of Rootâ™s capabilities accessible in ways familiar with anyone with experience in C++ programming or using other Unix-based applications.

Because Root is being developed for high energy physics (HEP), most of its capabilities are strongly directed at analyzing the output of such experiments like the LHC, often at the expense of many other basic statistical functionality that a statistician will have come to expect as standard. Particle accelerator experiments generate data that made up of large amounts of noise and small amounts of signal. The primary aim of Root is to identify that signal data, which may indicate important and elusive particles. As such, the majority of Root is devoted to univariate data.

3.2 Athena Framework

Offline computing covers all processing from storing raw data up to the final analysis, as well as Monte Carlo generation, detector simulation and event display. Athena is the general framework for the ATLAS offline software, based upon the Gaudi architecture. The Athena code is based on the C++ language and uses all of its object oriented features.

Athena can be seen as a skeleton which provides most of the common functionalities and into which the developers can insert their own code. This way, the software developed in Athena can use many useful background classes (physical units manipulation, geometry entities, etc.), using prepared services for things such as loop over events.

ATLAS software is organized into a hierarchical structure of projects and packages. All packages are stored in an official CVS repository, which enables efficient sharing of source code among the members of a distributed development team. Each package has a Tag number which distinguishes between different versions. A project consists of a complete collection of tagged packages and it is identified with a release number.

A Configuration Management Tool (CMT) is used to manage, build (compile and link) and run ATLAS software. The information needed to build or run a package is grouped in a single requirements file, from which CMT sets automatically the configuration parameters required to operate the packages.

The Athena framework distinguishes between data objects and algorithm objects very strictly. A quantity- like entities (hits, points, tracks, digits, raw channels, etc.) should be implemented by deriving their class from the DataObject base class. On the other hand anything like a procedure should be designed as a child class of the Algorithm base class.

Chapter 4

Event Selection

4.1 Event Selection Criteria for Bose-Einstein Correlations

The data used for this analysis consist of about 10^6 events recorded by ATLAS in March, April and May 2010 with a minimun-bias trigger, using about 584 μb^{-1} of 7TeV centre of mass energy proton-proton collisions provided by the LHC. A MinBias MC sample was also produced with Pythia, using the full detector simulation.

We require all tracks to have at least 2 Pixel and 2 SCT hits with $p_T > 200$ MeV and particle pseudorapidity to be $|\eta| < 2.5$. We exlude secondary particles coming from the decay of long-lived hadrons (K_s^0, Λ, etc.) and apply a cut of $\chi^2/N_{dof} < 5$. Finally, we excluded all pion pairs with relative angles less than 15^o in order to reduce e^+e^- pairs.

4.2 Armenteros-Podolanski Analysis

To ensure that our samples were free from pions coming from K_s^0 or Λ we used the Armenteros-Podolanski plot (see appendix B). The Armenteros plot is used in the analysis of the dynamics of two-body V decays.

For the three boson correlations we used the method of event mixing because we needed a sample free from any correlations and resonances. We applied an extra cut and accepted only events with a relative charge balance of $|(n^+ - n^-)|/(n^+ + n^-) < 0.25$, where n^+ and n^- are respectively the observed numbers of positevely and negatively charged tracks.

4.3 Coulomb Corrections

The final state of a charged pion pair is affected by the Coulomb force. Two like-charged pions experience Coulomb repulsion, producing fewer pairs in the region of small relative

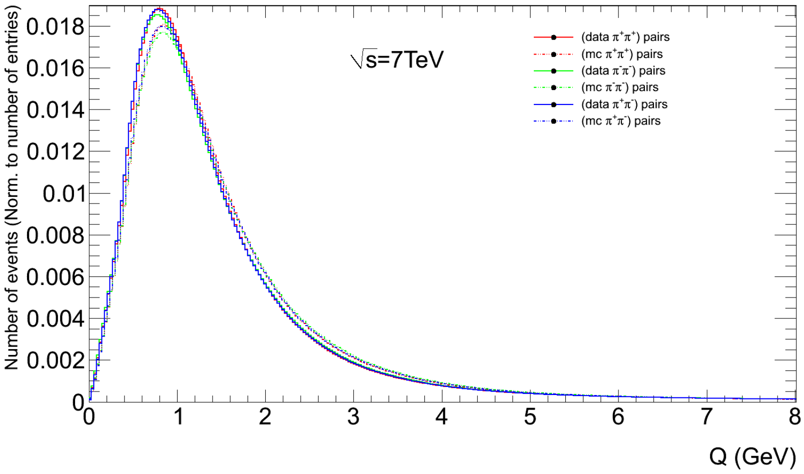

Figure 4.1: Q distributions of pion pairs. Continuous line corresponds to pairs from data, dashed to pairs from Monte Carlo. All distributions are normalized to number of entries.

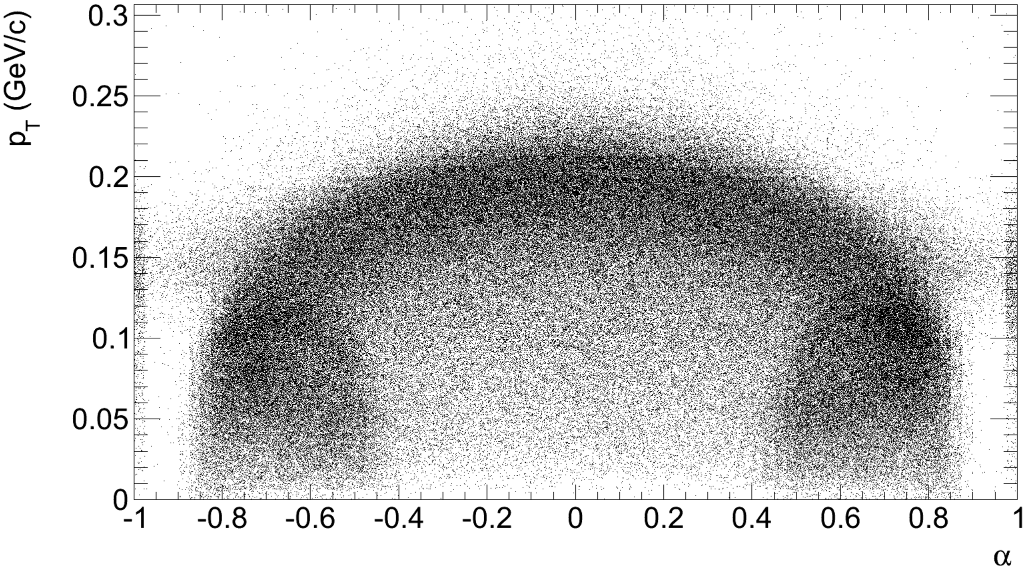

Figure 4.2: Curves for Λ, $\bar{\Lambda}$ and K_s^0 from ATLAS data.

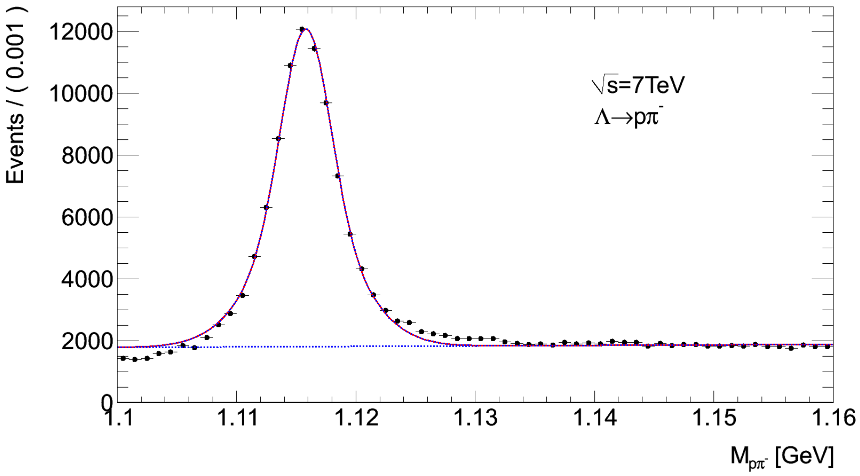

Figure 4.3: Λ mass spectrum in data.

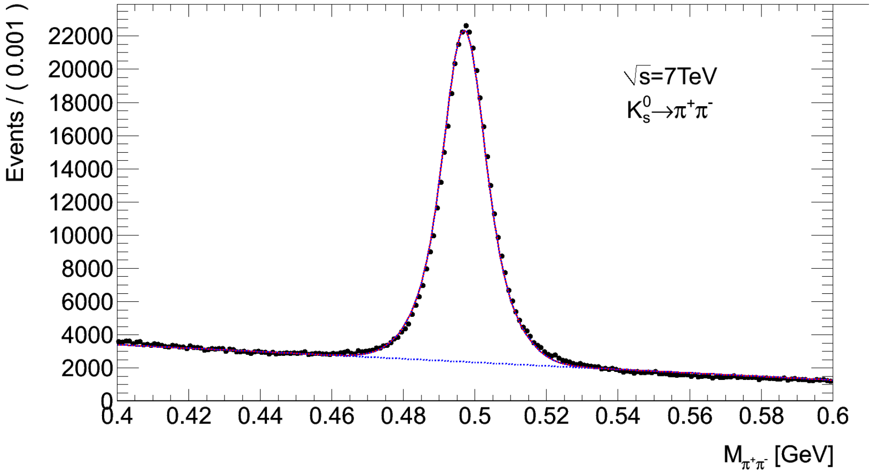

Figure 4.4: K_s^0 mass spectrum in data.

momenta. Unlik-charged pions will produce extra pairs. The correction factor for this effect follows the Gamow factor. The ratio of the corrected like to corrected unlike pairs then repsresents R in the absence of the Coulomb interaction.

For like and unlike charged pairs the inclusive distribution in the presence of the pair Coulomb interactions is given by $P_l(k_1, k_2) = G_l(\eta)P_n(k_1, k_2)$ for like and $P_u(k_1, k_2) = G_u(\eta)P_n(k_1, k_2)$ for unlike pairs, where $P_n(k_1, k_2)$ is the pair inclusive distribution in the absence of the Coulomb force, and

$$G_l(\eta) = \frac{2\pi\eta}{e^{2\pi\eta} - 1} \ , \tag{4.1}$$

$$G_u(\eta) = \frac{2\pi\eta}{1 - e^{-2\pi\eta}} \ , \tag{4.2}$$

$$\eta = \frac{\alpha m_\pi}{|k_1 - k_2|} \tag{4.3}$$

Here, $\alpha = \frac{1}{137}$ and k_1 and k_2 are pion four-momenta in the pair center-of-mass frame, so $\eta = \frac{\alpha m_\pi}{\sqrt{Q^2}}$.

Since we use three kinds of charged particles the Gamow correction is given by

$$C_1 = G_l(\eta_{12})G_l(\eta_{23})G_l(\eta_{31}) \ . \tag{4.4}$$

The unlike sample ($\pm\pm\mp$) triplet is corrected using

$$C_2 = G_l(\eta_{12})G_u(\eta_{23})G_u(\eta_{31}) \ . \tag{4.5}$$

So we correct each like-charged triplet with $1/C_1$ and each $\pm\pm\mp$ triplet with $1/C_2$.

4.4 Event Selection Criteria for $Z^0 \to \mu^+\mu^-$ Candidates

Collision events are selected by requiring at least one reconstructed primary vertex (PV) with a position $|z_{PV}| < 100$ mm and $|d_{0PV}| < 50$ mm relative to the nominal interaction point and at least 3 inner detector tracks associated with the PV. Each of the 3 tracks should have at least 1 hit in the pixel detector and at least 6 hits in the SCT.

To select collision events with muon final state we require combined muons with at least 1 hit in the pixel detector, 6 hits in the SCT and 1hit in the TRT. Pseudorapidity $|\eta| < 2.5$.

The selection of the $Z^0 \to \mu^+\mu^-$ decays is done by requiring two combined muons, with opposite electric charge, each satisfying the criteria above. Finally each of the selected muons should have a transverse momentum $p_T > 20$ GeV and be isolated[1] and a direction within the same η region.

---

[1] A muon is considered isolated if the sum of the transverse momenta of the (non-muon) tracks in a cone of $\sqrt{\Delta\eta^2 + \Delta\phi^2} = 0.4$ around the muon is less than 20% of the muon p_T.

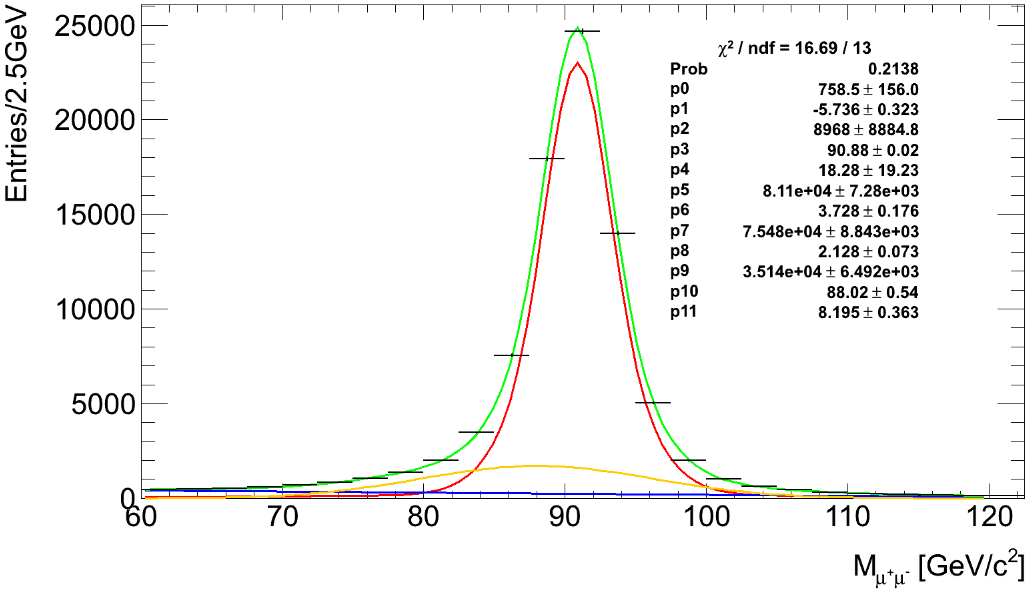

Figure 4.5: $\mu^+\mu^-$ invariant mass using ATLAS data. The distribution is fitted with a triple gaussian for the signal (marked with red), a gaussian for the radiative tail (marked with orange) and a polynomial for the background (marked with blue).

4.5 Fit Models

4.5.1 Bose-Einstein

The resulting Bose-Einstein ratio is fitted with two functions, whose parameters r and λ describe the particle source. All data samples were fitted with the following functions:

1. $1 + \lambda e^{-rQ^2}$,
2. $\left(1 + \lambda e^{-rQ^2}\right) / (1 + \delta Q^2)$

All fits are binned maximum likelihood fits.

4.5.2 $Z^0 \rightarrow \mu^+\mu^-$

For the $\mu^+\mu^-$ invariant mass spectrum a three gaussian distribution was used for the signal, a polynomial for the background and a gaussian for the radiative tail on the left of the peak.

The ρ distributions are fitted with simple gaussians.

Chapter 5

Results

5.1 Bose-Einstein Correlations

5.1.1 Two Pion Model

We used another three procedures to create different reference samples. All three of them were applied to same sign pion pairs from different events. The first reference sample contains pion pairs, with the three momentum of one of particles inverted, $(\vec{E}, \vec{p})$ changed to $(\vec{E}, -\vec{p})$. The second contains pion pairs coming from events where the invariant mass of all charged particles was similar to the events used for the signal sample. Last we used pairs coming from events with similar charged track multiplicity.

Using the function energy difference, described above, and the the fit function $C_2 = 1 + \lambda e^{-\alpha q_0^2}$, where $\alpha = \tau^2/\hbar^2 c^2$, we measured the lifetime τ. We examined the behaviour of τ for different multiplicities.

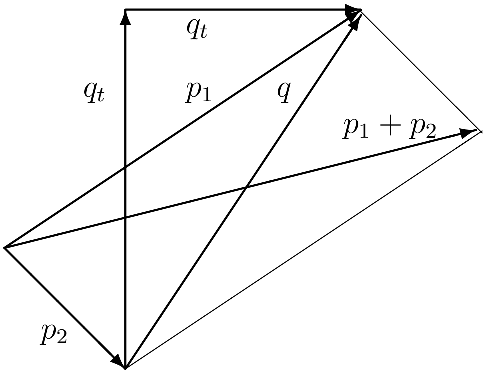

Figure 5.1: Total momentum $\vec{p}$, $\vec{q_t}$ and $\vec{q_l}$ vector definitions of a $\pi\pi$ pair.

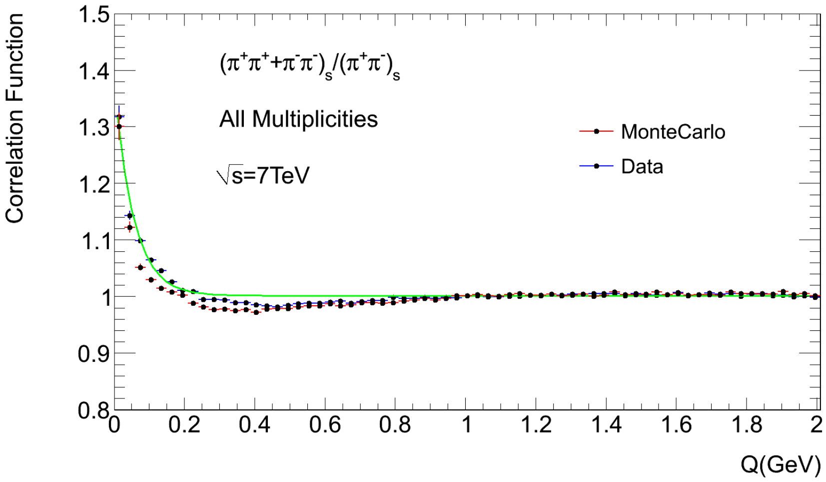

Figure 5.2: Ratio of like/unlike-sign pion pairs from both data and Monte Carlo.

Results of fits to 7TeV data

Multiplicity	λ	τ (fm)
2-9	0.862 ± 0.022	0.570 ± 0.014
10-14	0.566 ± 0.019	0.605 ± 0.018
15-19	0.455 ± 0.015	0.620 ± 0.019
20-29	0.382 ± 0.009	0.640 ± 0.014
30-39	0.298 ± 0.008	0.657 ± 0.011
40-79	0.247 ± 0.004	0.728 ± 0.010

5.1.2 Higher Order Model

Results of fits to 7TeV data

Fit Function	Order of Correlation	λ	r (fm)	$\delta(GeV^{-1})$
I	Second	0.379 ± 0.003	1.443 ± 0.008	-
	Third	1.077 ± 0.012	0.934 ± 0.046	-
	Fourth	1.866 ± 0.025	0.605 ± 0.031	-
II	Second	0.342 ± 0.003	1.267 ± 0.016	-0.008 ± 0.000
	Third	1.038 ± 0.014	0.887 ± 0.049	-0.010 ± 0.000
	Fourth	2.359 ± 0.032	0.668 ± 0.003	-0.002 ± 0.000

5.1.3 Multiplicity Dependence

The multiplicity dependence of the obtained HBT radius was examined by studying events with track multiplicity: (a) two to ten tracks, (b) ten to fifteen, (c) fifteen to twenty, (d)

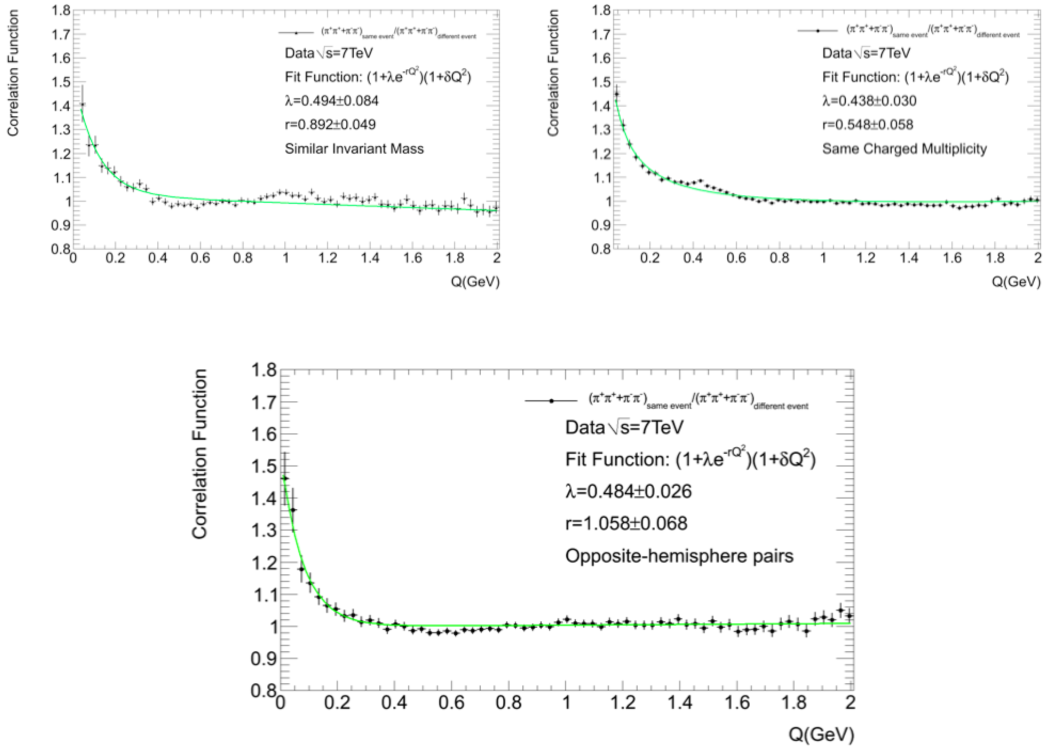

Figure 5.3: Ratio of like-sign pion pairs from save event to pairs from different events using different reference samples. Top left: Inverted three momentum, Top Right: Pairs from events with similar multiplicity, Bottom: Pairs from events with similar invariant mass.

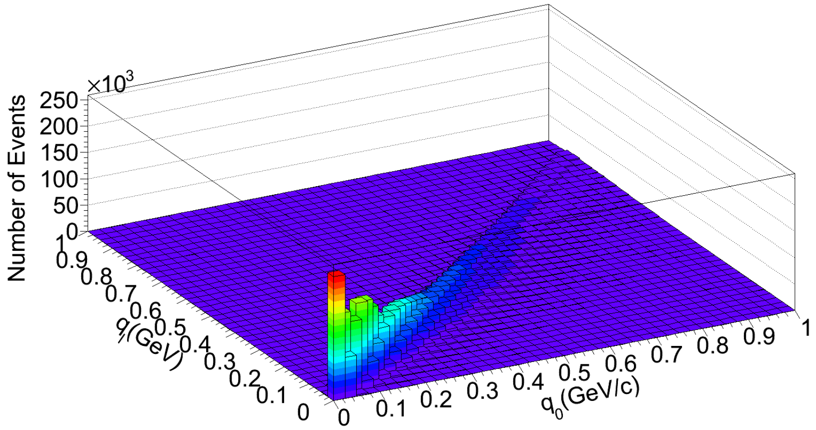

Figure 5.4: Relation of q_0 versus q_l

twenty to thirty, (e) thirty to fourty and (d) fourty to eighty.

Results of fits to 7TeV data

Fit Function	Multiplicity	$< N_{tracks} >$	λ	r (fm)	$\delta(GeV^{-1})$
I	2-9	5.3	1.192 ± 0.031	0.888 ± 0.017	-
	10-14	11.9	0.860 ± 0.024	0.985 ± 0.020	-
	15-19	16.9	0.722 ± 0.020	1.054 ± 0.021	-
	20-29	24.1	0.678 ± 0.014	1.279 ± 0.018	-
	30-39	34.2	0.560 ± 0.013	1.451 ± 0.022	-
	40-79	55.6	0.436 ± 0.007	1.582 ± 0.016	-
II	2-9	5.3	1.171 ± 0.031	0.787 ± 0.018	-0.050 ± 0.002
	10-14	11.9	0.847 ± 0.021	0.822 ± 0.017	-0.039 ± 0.002
	15-19	16.9	0.703 ± 0.018	0.889 ± 0.018	-0.028 ± 0.001
	20-29	24.1	0.572 ± 0.012	0.958 ± 0.036	-0.020 ± 0.002
	30-39	34.2	0.516 ± 0.010	1.162 ± 0.018	-0.017 ± 0.000
	40-79	55.6	0.414 ± 0.006	1.408 ± 0.017	0.006 ± 0.000

5.1.4 Systematic Checks

In order to check if the enhancements we have measured are not the result of a systematic analysis error, we have applied our analysis to another data sample. The same procedures and data cuts were used as described in 2.1.

We used pion pairs of unlike sign ($\pi^+\pi^-$) in both the same event and different event combinations. This study was performed to two different sets of samples; one with charged

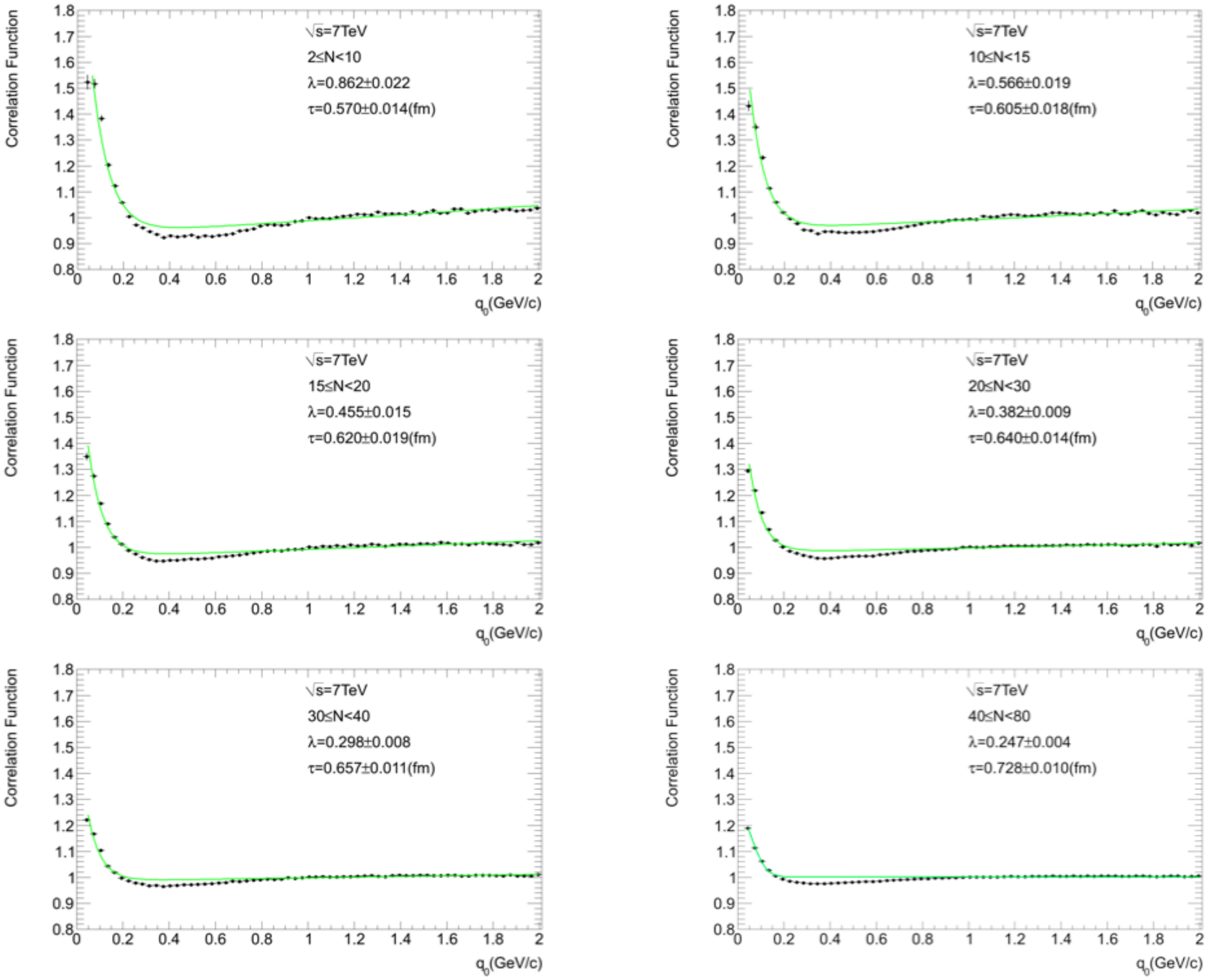

Figure 5.5: Lifetime as a function of charged particle multiplicity. Fitting functions shown are $1 + \lambda e^{-\alpha q_0^2}$

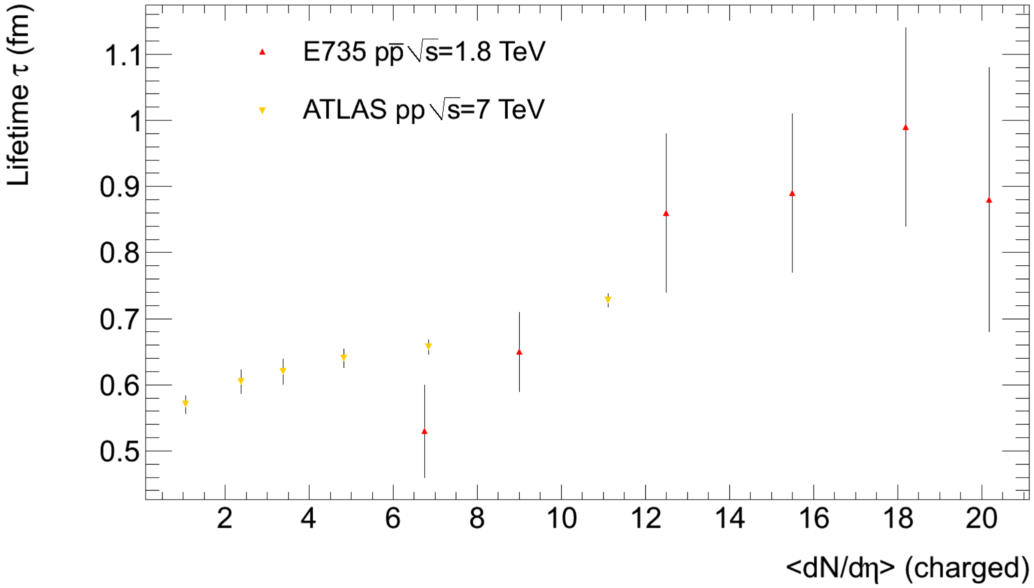

Figure 5.6: Gaussian lifetime (τ) conjugate to q_0 as a function of charged particle multiplicity per unit of pseudorapidity ($dN/d\eta$). Measurements from E735 and ATLAS experiment.

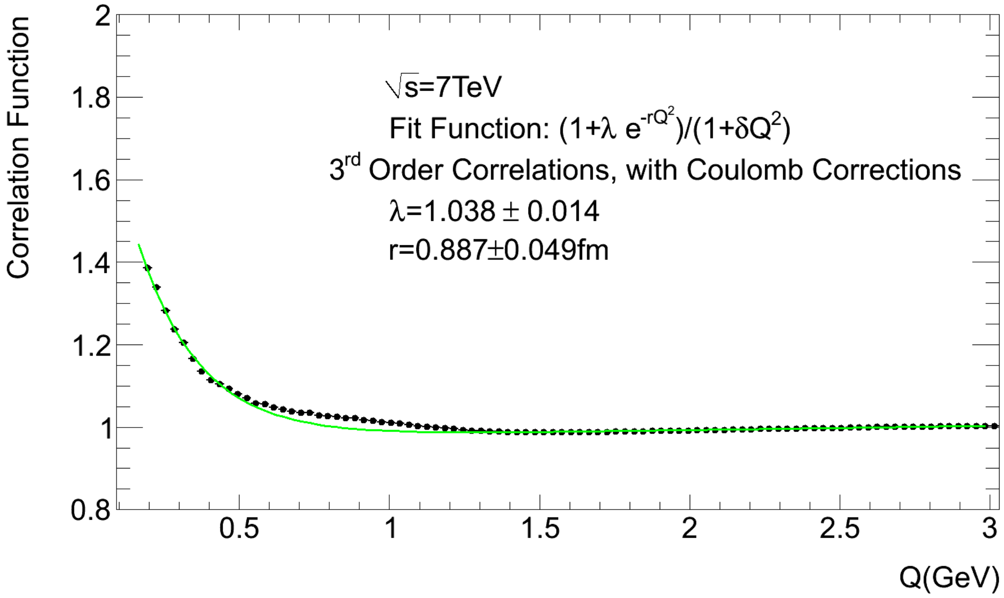

Figure 5.7: 3^{rd} order boson correlations.

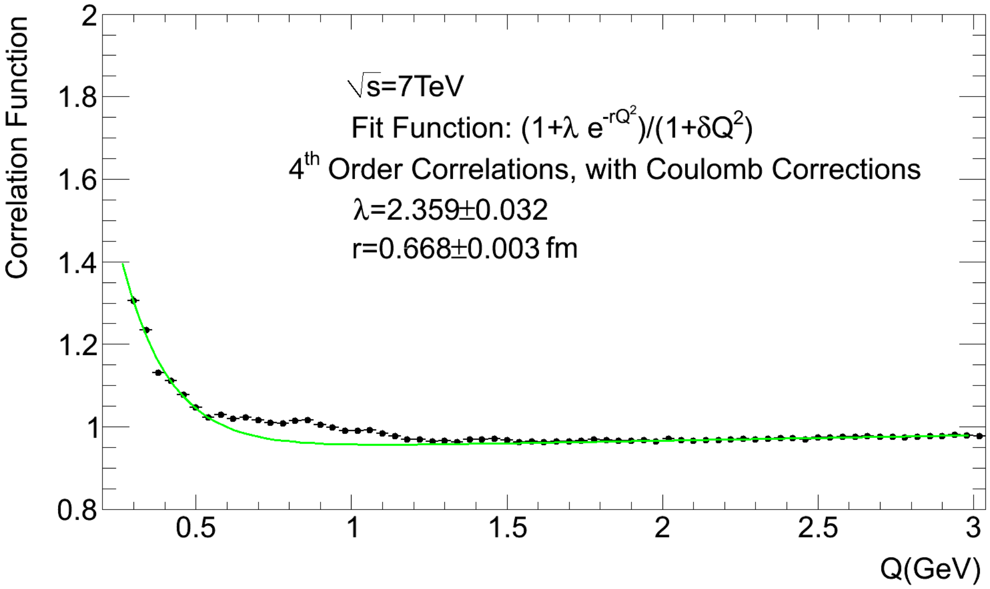

Figure 5.8: 4^{th} order boson correlations.

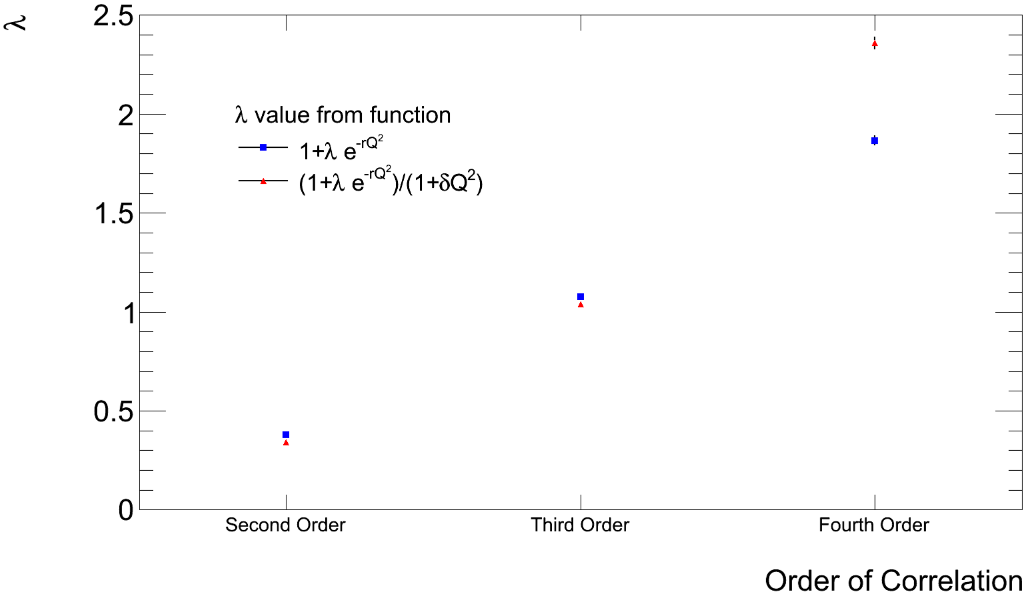

Figure 5.9: Value of λ parameter as a function of the correlation order.

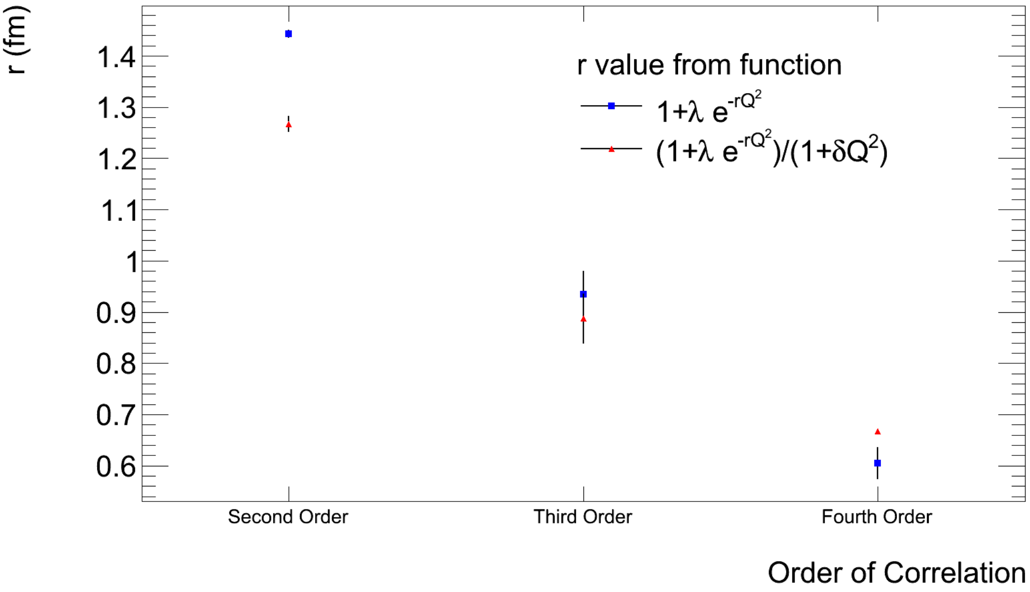

Figure 5.10: Value of r parameter as a function of the correlation order.

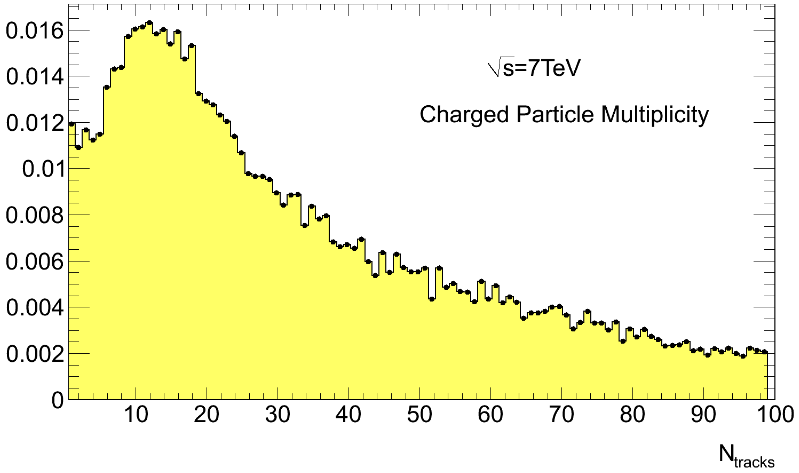

Figure 5.11: Charged particle multiplicty normalized to number of entries.

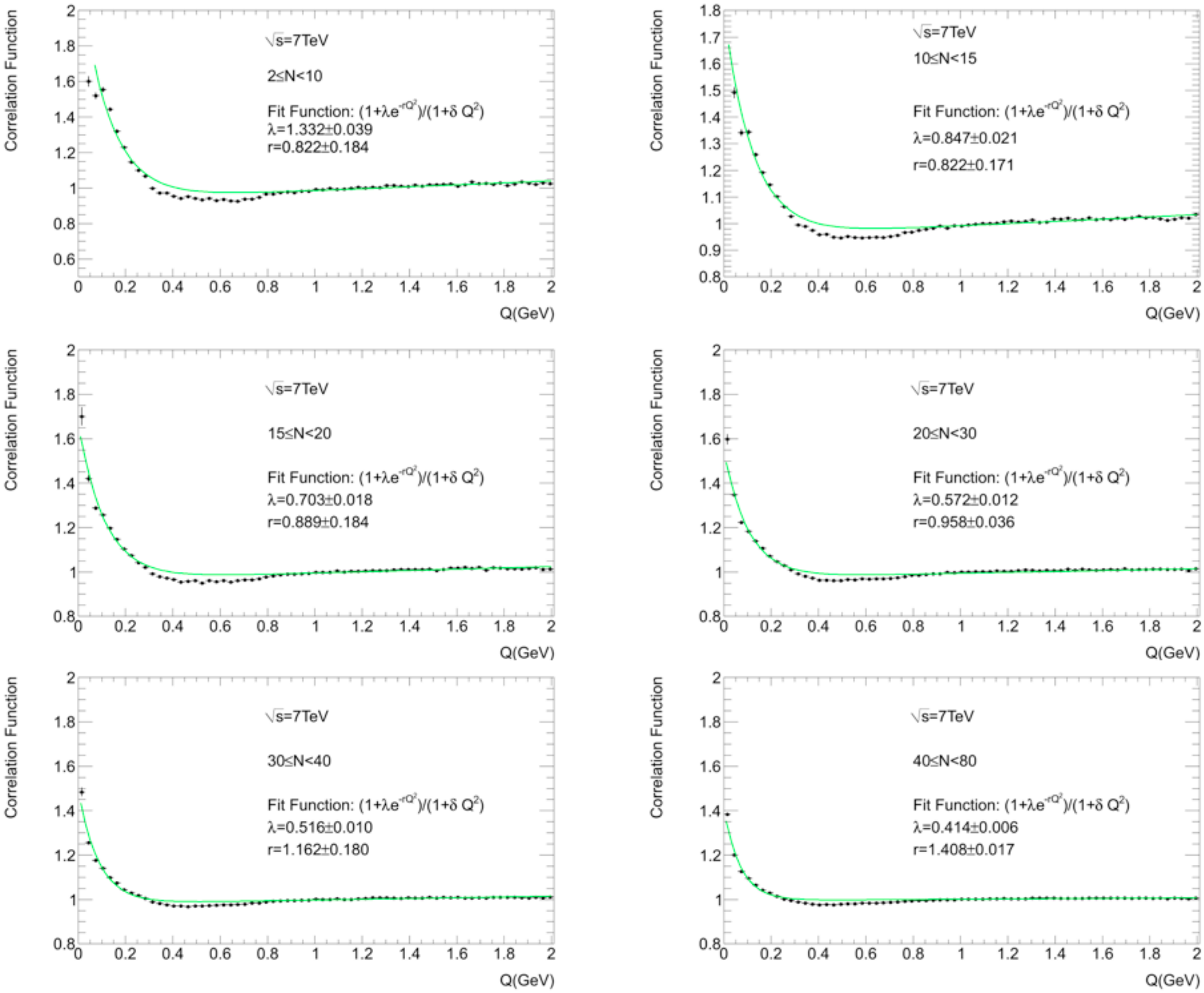

Figure 5.12: Second order correlations for different charged particle multiplicities. Fitting functions shown are $(1 + \lambda e^{-rQ^2})(1 + \delta Q^2)$

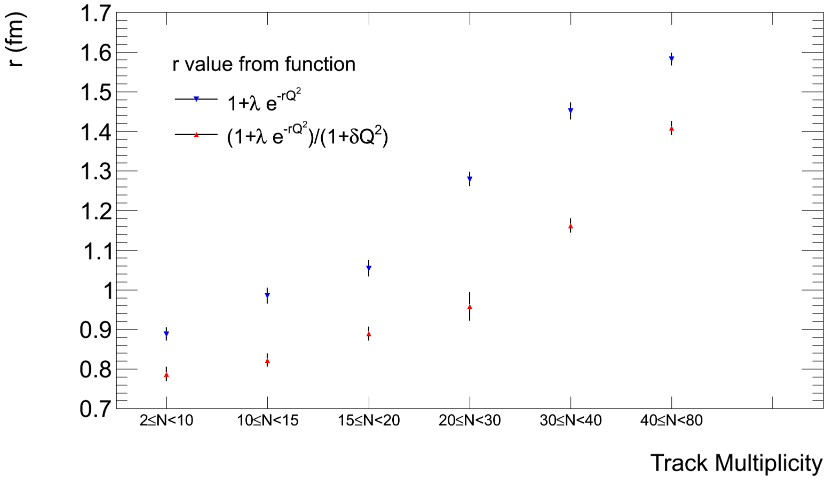

Figure 5.13: Value of r parameter as a function of the charged particle multiplicity.

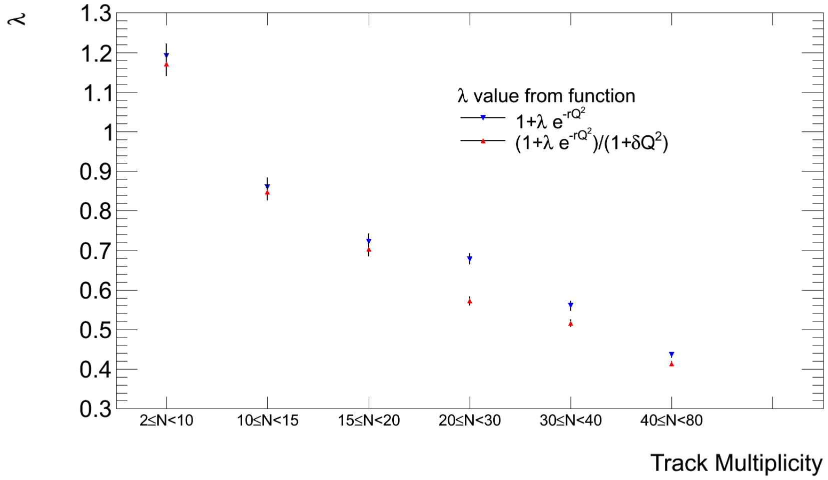

Figure 5.14: Value of λ parameter as a function of the charged particle multiplicity.

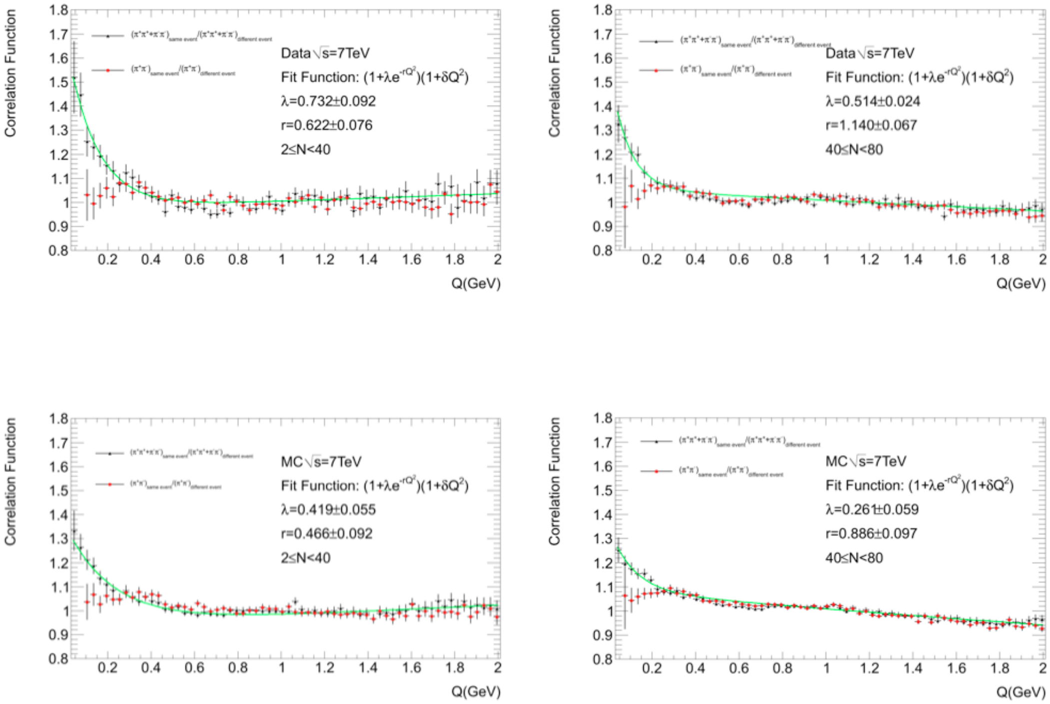

Figure 5.15: Correlation function for like and unlike sign pion pairs for two set s of multiplicities ($2 \leq N < 40$ and $40 \leq N < 80$). Analysis applied to data and Pythia MC with Bose-Einstein correlation.

track multiplicty between two and fourty and one with track multiplicity between fourty and eighty. None systematic enhancement was observed. We performed the same technic of mixing events for like sign pion pairs ($\pi^+\pi^+ + \pi^-\pi^-$) were we expected and observed Bose Einstein correlations.

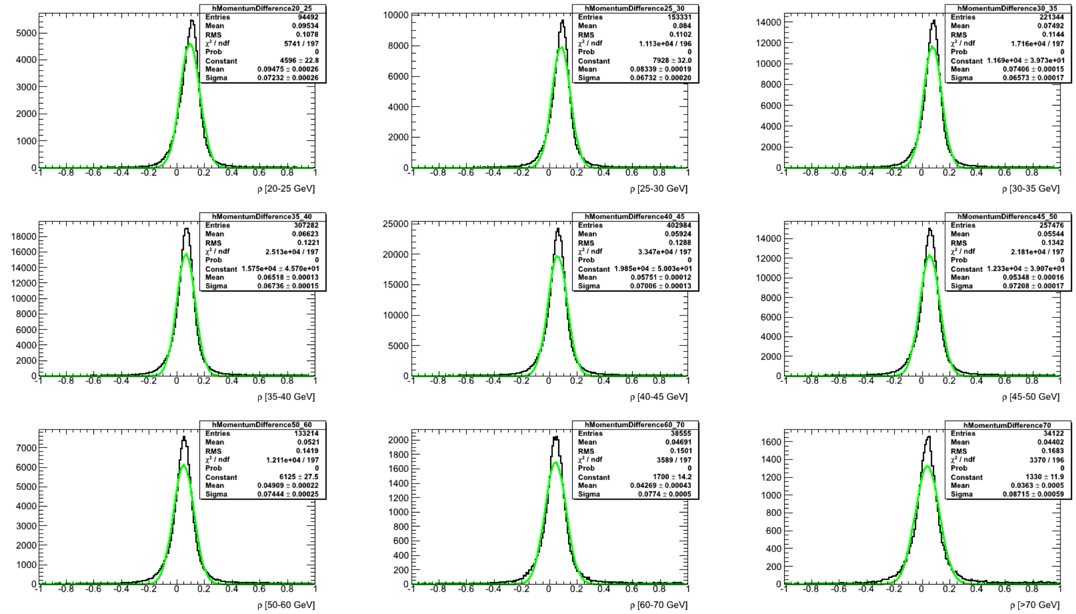

Figure 5.16: ρ distributions for various p_T ranges

5.2 Muon Spectrometer Performance Studies with $Z^0 \to \mu^+\mu^-$

A way of measuring the muon momentum resolution is to use the redundancy in the ATLAS tracking systems, by comparing the independent momentum measurements for events with single muons. A relative difference in momentum is defined as

$$\rho = \frac{p_{\mathrm{ID}} - p_{\mathrm{MS}}}{p_{\mathrm{ID}}} \,, \tag{5.1}$$

where p_{ID} denotes the momentum measurement in the ID and p_{MS} the momentum measured by the MS and extrapolated to the interaction point, taking energy loss into account. As a result the expectation value for ρ is 0. Depending on the region of the pseudorapidity and the range of p_{T}, this quantity is dominated by the ID or MS contribution.

To extract the resolution as a function of the muons p_{T} the ρ distribution is fitted with a gaussian distribution. Having the advantage of large statistics (3.24 fb^{-1}) we perform the fitting procedure in nine p_{T} bins: $20-25$ GeV, $25-30$ GeV, $30-35$ GeV, $35-40$ GeV, $40-45$ GeV, $45-50$ GeV, $50-60$ GeV, $60-70$ GeV and > 70 GeV. By fitting the distributions of ρ we plot the σ's and the μ's of the fits as a function of p_T.

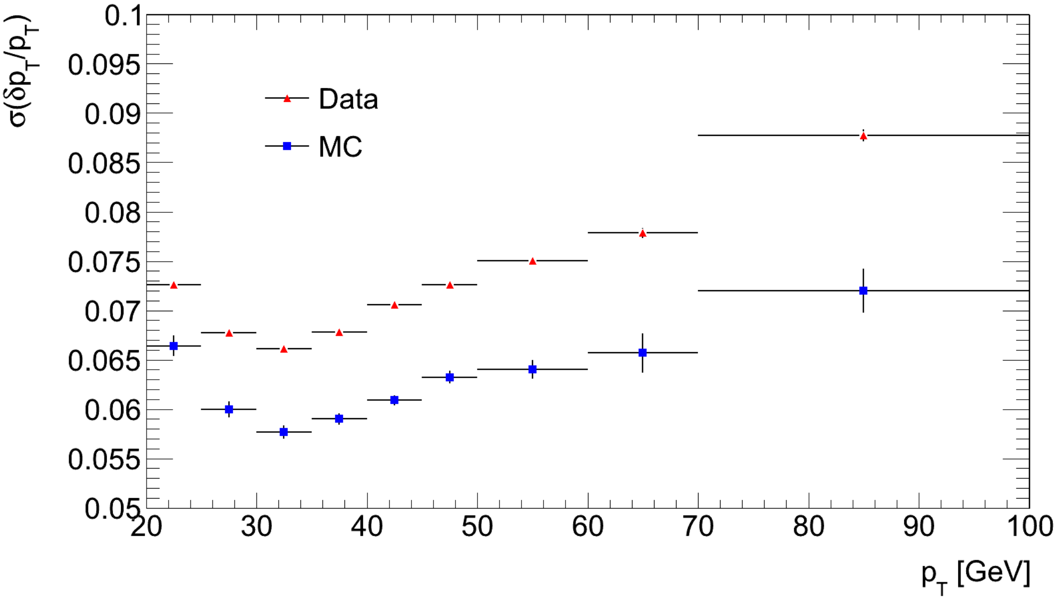

Figure 5.17: σ's of the distributions of ρ as a function of p_T

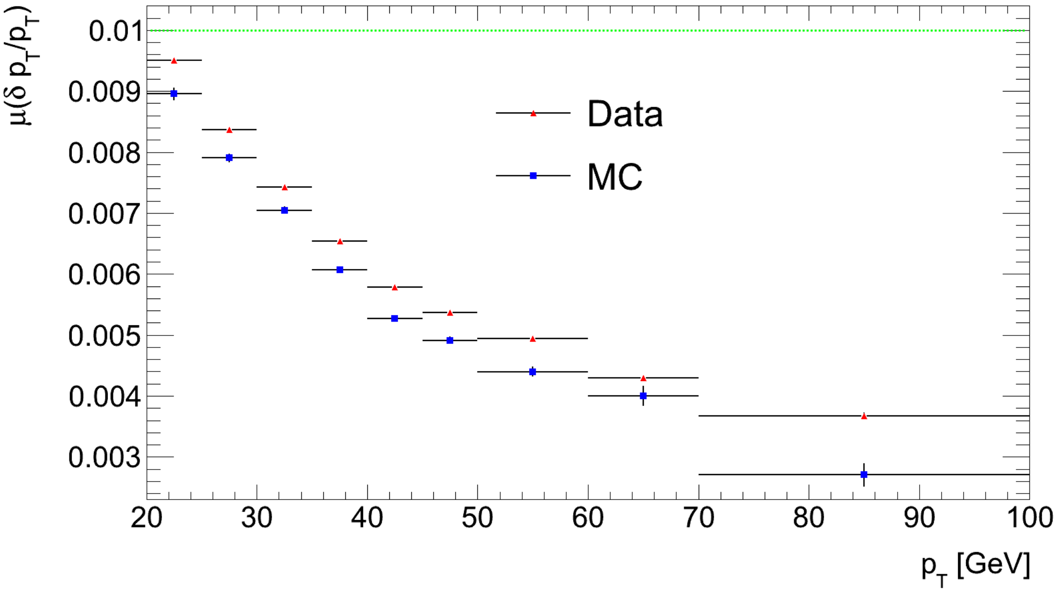

Figure 5.18: μ's of the distributions of ρ as a function of p_T

Chapter 6

Conclusions

The ATLAS experiment measured Bose-Einstein correlations in proton proton interactions. The results emerging from our analysis show that the size of the pion source is about 1 fm and depends on the charged track multiplicity, (it's value rises as the event multiplicity rises). Lifetime (τ) also measured around an approximate value of about 0.6 fm and behaves likewise with r. The strength of the chaoticity effect (λ) is almost the same when is determined by fits either for r or τ and decreases as the multiplicity increases.

A comparison of our results with those of other experiments shows a good agreement, demonstrating that the features of the final state hadronization processes have little dependence on the type or energy of the interacting particles.

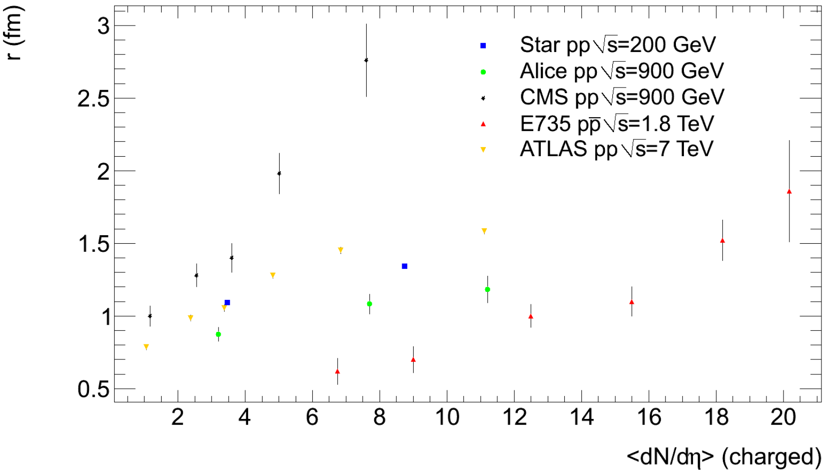

Figure 6.1: The multiplicity dependence of the radius r from hadronic collisions measured by STAR, ALICE, E735 and ATLAS.

Chapter 7

Target Reconstruction with the MicroMeGas Detector

In this chapter I apply two methods using clusters at three MicroMeGas chambers (R14, R19M and R19G) for target reconstruction.

7.1 Event Selection

The data analyzed were gathered in CERN's test beam facility (H6) during June 2011. In this test beam three MicroMeGas chambers were used (R14, R19M and R19G) in the setup as shown in fig 7.1. The trigger logic that was used to record the events from the pion beam can be found in figure **??**.

The characteristics of each chamber can be found in table 7.1. The gas that was used was $\mathrm{Ar} : \mathrm{CO}_2, 93 : 7$.

Name	Width [mm]	Length [mm]	Height [mm]	Amplification Gap [μm]	Drift Gap [mm]	Strip Pitch	Strip Width	Strip Length
R14	200	200	20	128	5	250	150	80
R19M	200	200	20	128	5	x:350	x:300	80
						u:900	u:100	
						v:900	v:100	
R19G	200	200	20	178	5	x:350	x:300	100
						u:900	u:100	
						v:900	v:100	

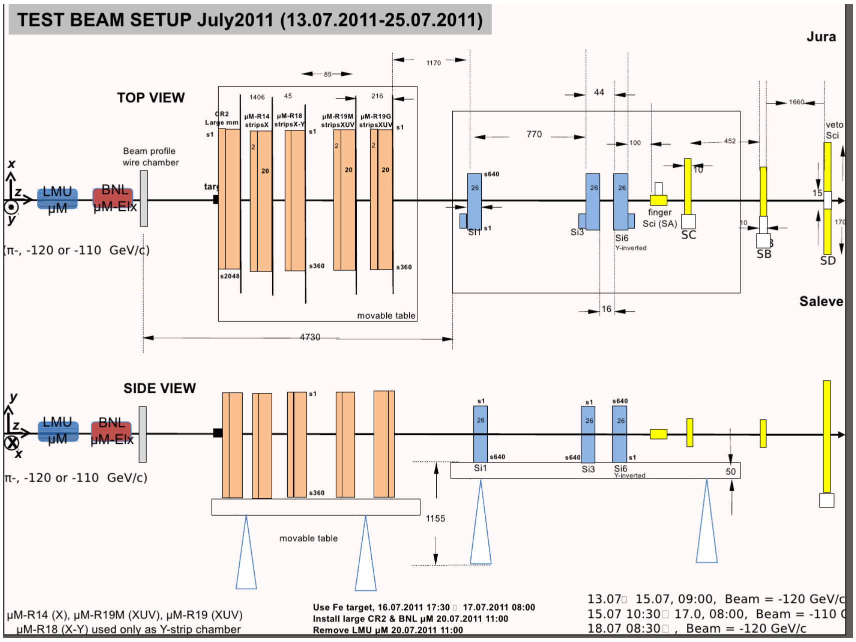

Figure 7.1: Setup of the R14, R19M and R19G MicroMeGas chambers.

7.2 Method A

Theory

We use cluster positions in three MicroMegas Chambers to reconstruct the event vertex. For any pair of clusters (requiring the clusters to be in different chambers), we reconstruct the intercept of the line that connects these two chamber clusters with the beam line. This intercept, x_v, is given by:

$$x_v = \frac{x_j(m)z_i(n) - x_i(n)z_j(m)}{z_i(n) - z_j(m)} \tag{7.1}$$

where $(z_i(n), x_i(n))$, $(z_j(m), x_j(m))$ are the coordinates of cluster n, in plane i, and cluster m in plane j, respectively. Taking into account the chamber resolution for these two hits, a smearing (AB) of the intercept x_v can be defined

$$(AB) = 2\sigma \frac{z_i(n) + z_j(m)}{|z_i(n) - z_j(m)|} \tag{7.2}$$

where σ is the chamber cluster resolution. A Lorentzian function $L_{i,j}(n, m)$ is constructed for these two chamber clusters

$$L_{i,j}(n, m) = \frac{1}{(x - x_v)^2 + (AB)^2/4} \tag{7.3}$$

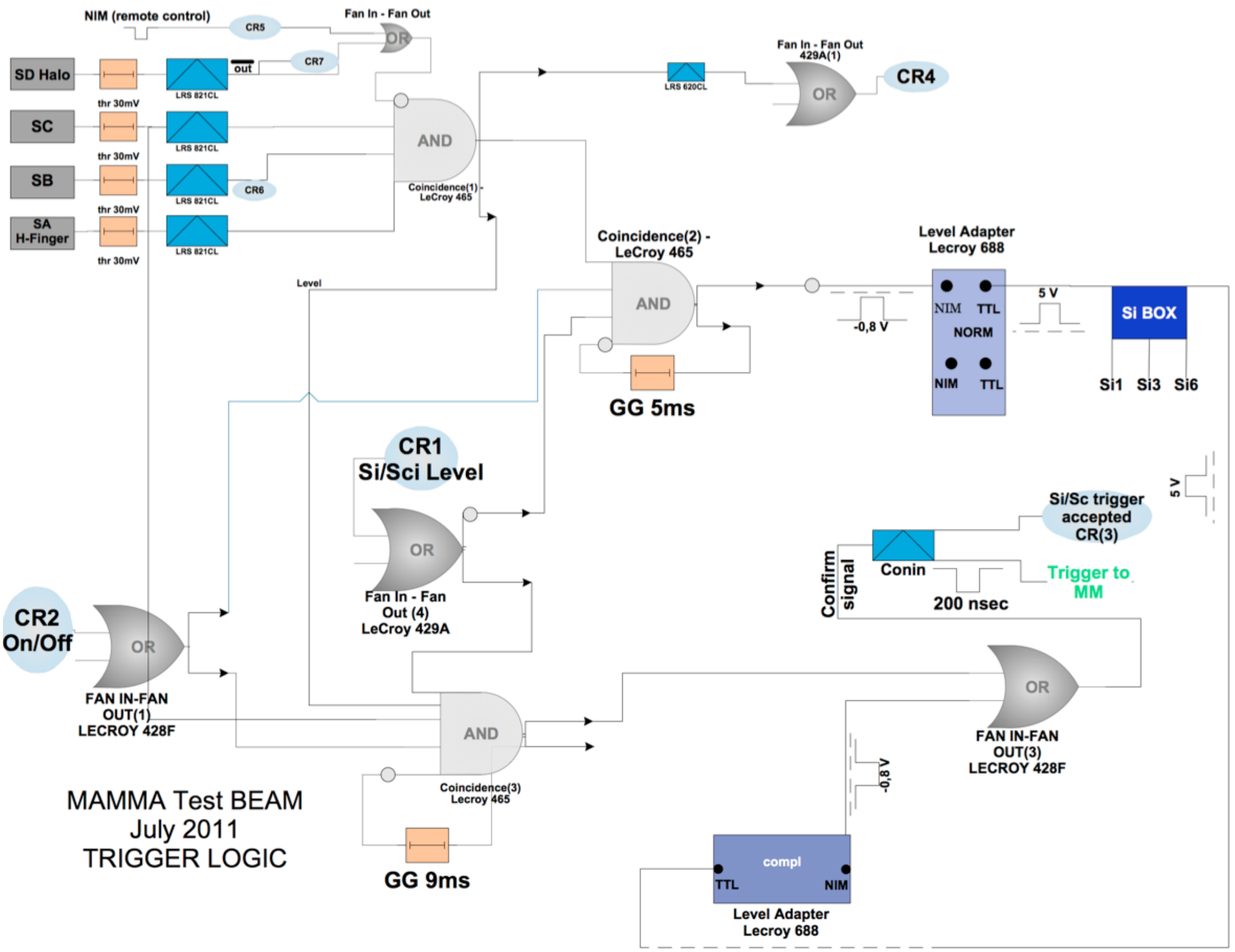

Figure 7.2: Trigger logic used for the test beam.

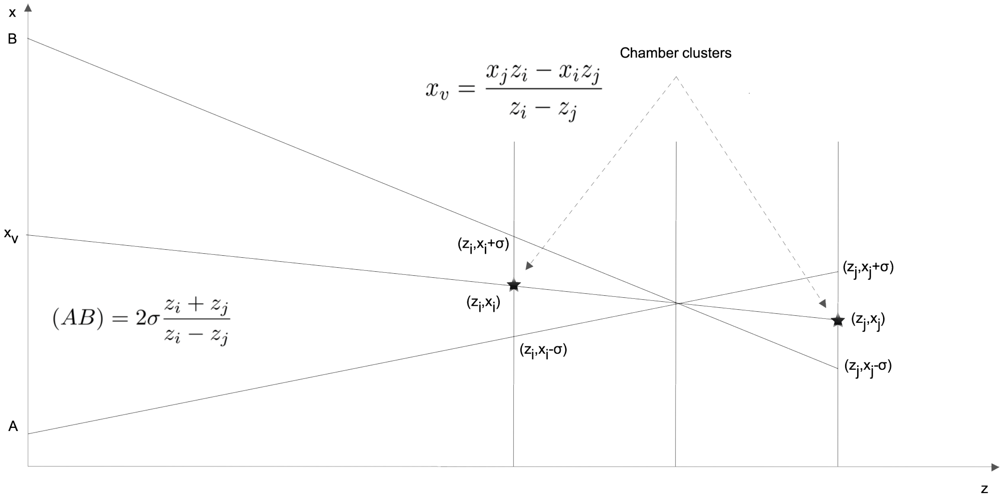

Figure 7.3: Two hits in the chamber and the definition of z_v and (AB).

where z_v and (AB) are defined as above. This procedure was repeated for each pair of clusters which were in different chambers. By summing all contributions, $L_{i,j}(n,m)$, for all possible clusters, we define a global function $G(x)$ which is the probability of the vertex point:

$$G(x) = \sum_{i}^{3} \sum_{j}^{3} \sum_{n}^{N_i} \sum_{m}^{N_j} L_{i,j}(n,m) \tag{7.4}$$

where N_i and N_j are the number of clusters in the chamber plane ($i = 1, , 3$), ($j = 1, , 3$), respectively. The maximum of the global function $G(x)$ defines the vertex of an event x_g. Figure 7.10 show the reconstruction of the event vertex for charged track multiplicity events.

After determining the determination of the x_v we use the same method in order to find the z_v.

7.2.1 Results

Monte Carlo

The determination of the vertex point, x_g, was studied using Monte Carlo methods. In this Monte Carlo simulation, a number of particles are generated uniformly and originating at a common vertex point, x_{gen}. Each particle is followed through the chambers to simulate chamber clusters. The vertex, x_{rec} is reconstructed from the simulated chamber clusters (assigning ambiguity clusters too) using method above. Figure **??** shows the $x_{gen} - x_{rec}$ distribution for a radial cluster resolution of $\sigma = 0, 150, 300$ and 500 μm. It seems this method reconstructs the vertex point, x_g. From this Monte Carlo study, one could con-

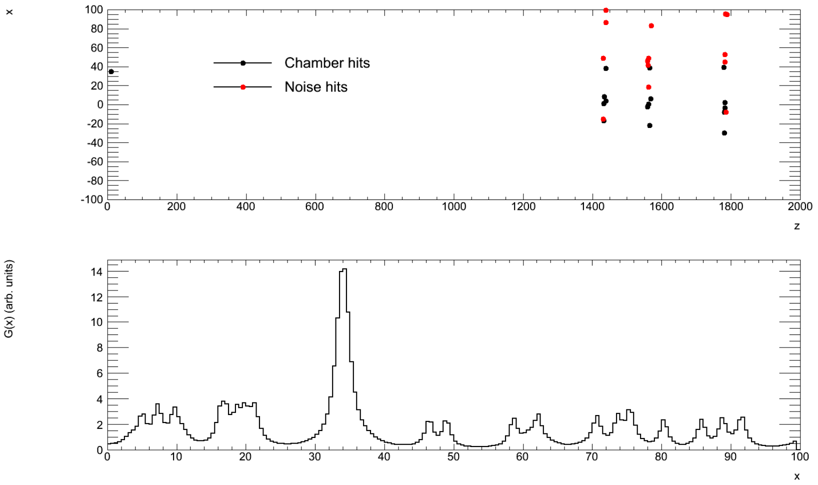

Figure 7.4: X-chamber points used to reconstruct the event vertex of a typical high multiplicity event using method A

clude that the vertex x_g or x_{rec} can be located to within $\pm 139.9\ \mu$m relative to the generated vertex point.

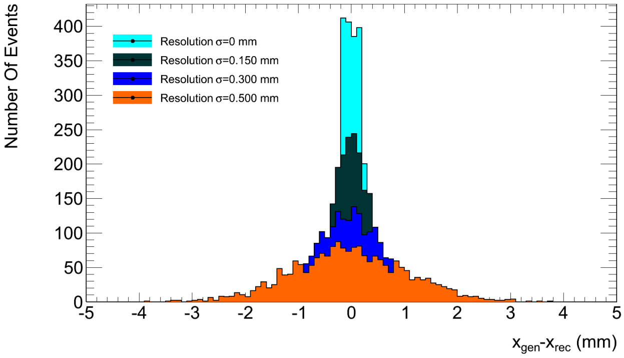

Figure 7.5: $x_{gen} - x_{rec}$ distribution using Monte Carlo data for chamber resolution $\sigma = 0,\ 150,\ 300$ and $500\ \mu$m.

Data

x-axis

We used the method described above on four different sets of data. Three data sets including events with a target positioned between the beam pipe and the chambers (with distances 1.43m, 1m and 0.5m) and one dataset including events taken without a target.

Applying the method to the run without the target we get the beam profile, as seen in picture 7.6.

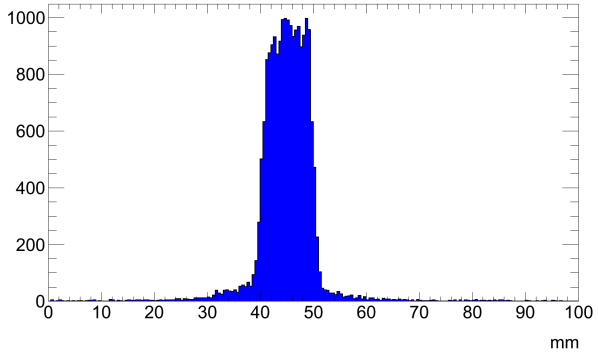

Figure 7.6: Beam profile.

Applying the method to the runs with the target, the beam profile gets broader, something expected as the particles scatter from the target.

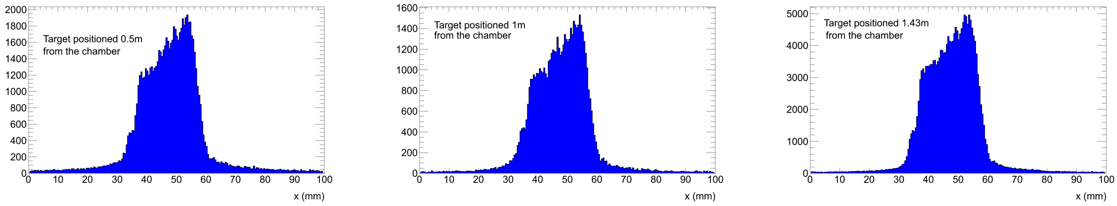

(a) Target positioned 0.5m from the chambers.

(b) Target positioned 1.0m from the chambers.

(c) Target positioned 1.43m from the chambers.

Figure 7.7: Beam profile for three runs, having a target positioned between the beam and the chambers in three different distances.

z-axis

Using the same method, having found the x_v we now try to point the z_v. Applying this method to the dataset without target we expect to see a flat distribution, as indeed is seen in figure 7.14.

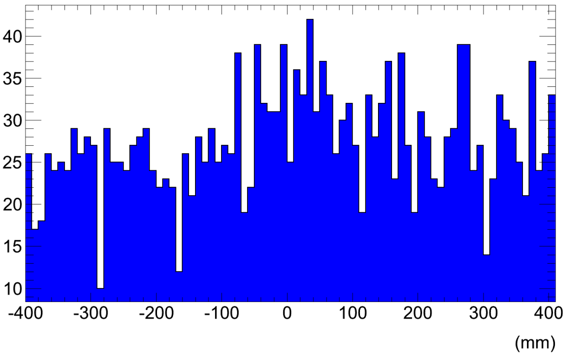

Figure 7.8: Flat distribution on z_v is expected, as there is no target between the beam and the chambers.

Analyzing the datasets with the target between the beam and the chambers we see a bump, indicating the existence of the target. This is show in the figures below.

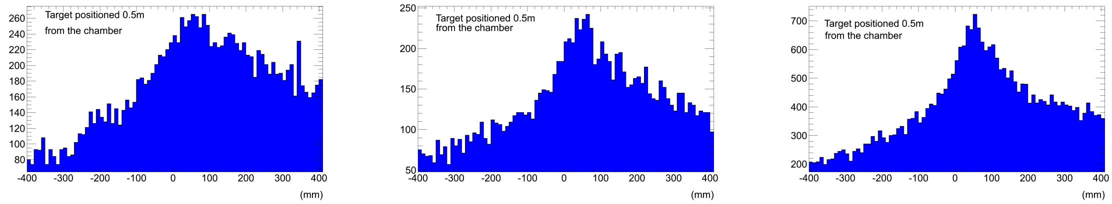

(a) Target positioned 0.5m from the chambers.

(b) Target positioned 1.0m from the chambers.

(c) Target positioned 1.43m from the chambers.

Figure 7.9: A peak starts to form in the scan of the z-axis, indication of the target that was positioned between the beam and the chambers.

7.3 Method B

7.3.1 Theory

Using a similar method as A, for two pairs of clusters (requiring the clusters for each pair to be in different chambers) we now construct a 2d gaussian in the point where the tracks from each pair intercept in the $x - z$ plane. Using this method we can now define the x_v and z_v position.

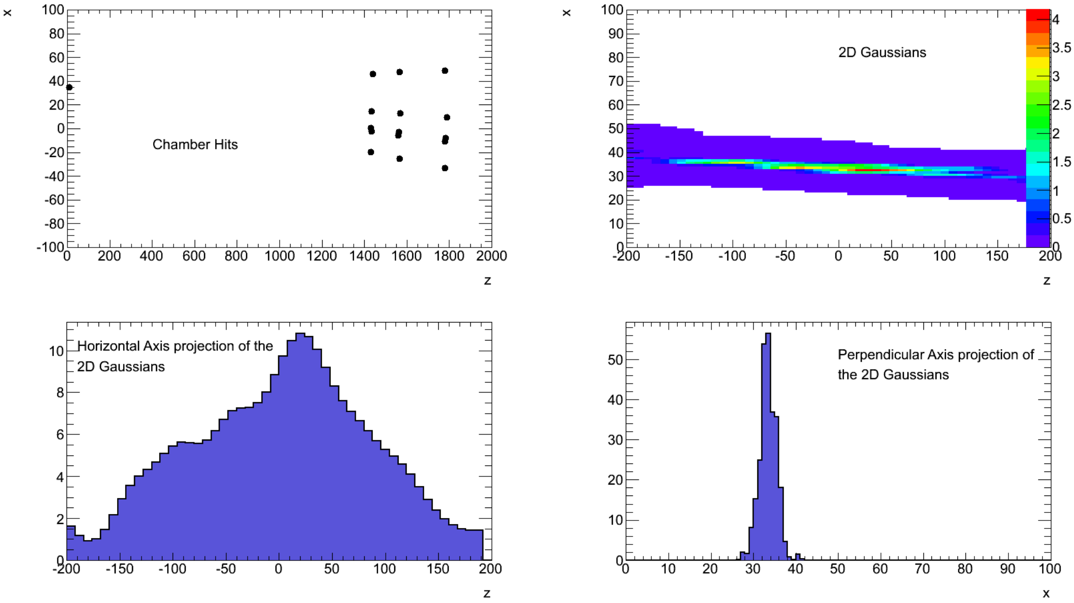

Figure 7.10: X-chamber points used to reconstruct the event vertex of a typical high multiplicity event using method B

7.3.2 Results

Monte Carlo

We created a Monte Carlo simulation, with the same conditions as in the previous method (1.2). Figure 7.11 shows the $x_{gen} - x_{rec}$ distribution for a radial cluster of $\sigma = 0,\ 150,\ 300,$ and $500\ \mu$m. This method, as well as the first, reconstructs the vertex point, x_g.

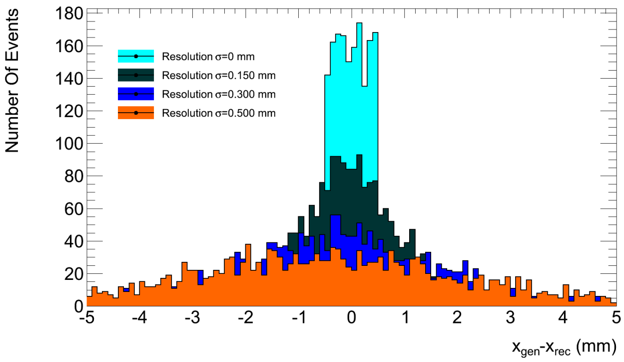

Figure 7.11: $x_{gen} - x_{rec}$ distribution using Monte Carlo data for chamber resolution $\sigma = 0,\ 150,\ 300$ and $500\ \mu$m.

Data

From the 2D gaussian we take the projections on the horizontal and perpendicular axis. For the runs without the target we expect a flat distribution for the z while for the x we expect the beam profile.

Applying this method to the runs with the target positioned between the beam and the chambers we get a wider beam profile and a bump in the z axis, indication of the target.

x-axis

Applying the method to the run without the target we get the beam profile, as seen in picture 7.12.

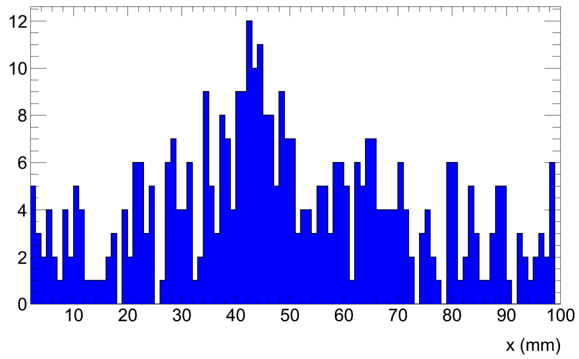

Figure 7.12: Beam profile.

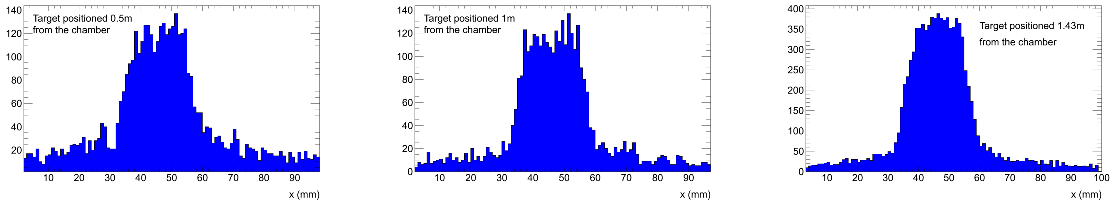

(a) Target positioned 0.5m from the chambers.

(b) Target positioned 1.0m from the chambers.

(c) Target positioned 1.43m from the chambers.

Figure 7.13: Beam profile for three runs, having a target positioned between the beam and the chambers in three different distances.

z-axis

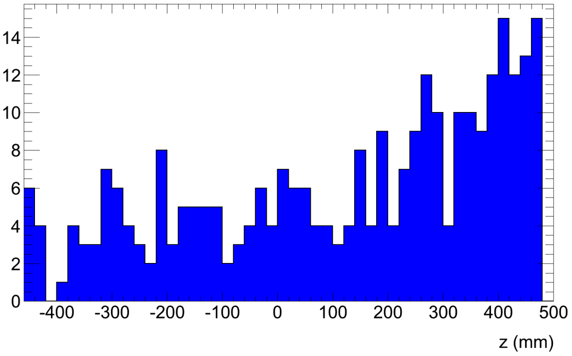

Figure 7.14: Flat distribution on z_v is expected, as there is no target between the beam and the chambers.

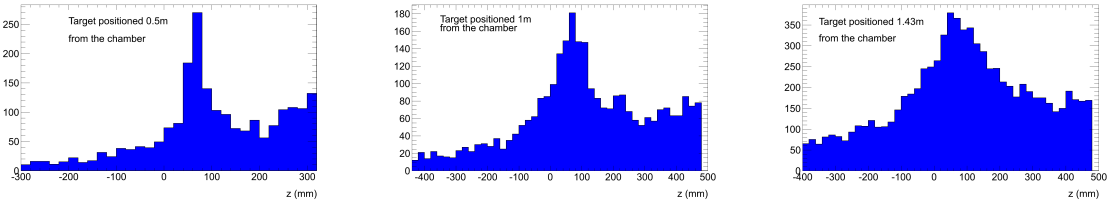

(a) Target positioned 0.5m from the chambers.

(b) Target positioned 1.0m from the chambers.

(c) Target positioned 1.43m from the chambers.

Figure 7.15: A peak starts to form in the scan of the z-axis, indication of the target that was positioned between the beam and the chambers.

Appendix A

Coordinate System and Nomenclature

The ATLAS experiment uses a right handed coordinate system, with the $z-$axis pointing along the LHC beam pipe, and the plane perpendicular to the beam pipe defines the $x-y-$plane. The positive $x-$axis is pointing from the interaction point towards the centre of the LHC, the positive $y-$axis is going upwards. The positive side of the $z-$axis is pointing towards the side A (direction Geneva) of the ATLAS detector, while negative $z-$values are assigned to the side C (direction Jura).

Due to the cylindrical symmetry of the ATLAS detector, the use of cylindric coordinates (ϕ, θ and R) is useful. In this coordinate system the transverse distance to the $z-$axis is defined as the radius R. The azimuthal angle ϕ is measured around the beam axis, starting with $\phi = 0$ on the $x-$axis and $\phi = \pi/2$ on the $y-$axis. Usually the azimuthal angle is defined within $\phi \in [-\pi, \pi]$. The polar angle θ is defined within $\theta \in [0, \pi]$, where $\theta = 0$ is on the positive $z-$axis. In terms of the particles momentum components p_x, p_y and p_z, the two angles ϕ and θ can be written as:

$$\tan\phi = \frac{p_x}{p_y}$$

$$\tan\theta = \frac{\sqrt{p_x^2 + p_y^2}}{p_z}$$

A more convenient way to express the polar angle θ is to use the pseudorapidity, which either can be expressed in terms of the polar angle or in terms of the particles momentum:

$$\eta = -\ln\left(\tan\frac{\theta}{2}\right) = -\frac{1}{2}\ln\left(\frac{|\boldsymbol{p}| - p_z}{|\boldsymbol{p}| + p_z}\right)$$

While the pseudorapidity is invariant under a Lorentz transformation, in the high energy limit of massless particles ($E >> mc^2$) the pseudorapidity becomes equal to the rapidity

$$y = \frac{1}{2}\ln\left(\frac{E - p_z}{E + p_z}\right)$$

which is Lorentz invariant under longitudinal boost. In addition, for the $x-y-$plane, η is equal to zero, in beam direction $\eta \to \pm\infty$ which corresponds to $\theta = 0$ and $\theta = \pi$.

In hadron collisions the trajectory of a particle is defined by various kinematic variables. The projection of the initial particles momentum p on the $x-y-$plane is defined as the transverse momentum p_T and the projection on the $z-$axis corresponds to the longitudinal momentum p_L. In the same manner the energy E can be split into the two components E_T and E_L. The transverse distance of the trajectories closest approach to the beam axis is defined as the transverse impact parameter d_0. Accordingly, the distance along the $z-$ axis to the closest approach to the interaction point is defined as longitudinal impact parameter z_0.

Appendix B

Z^0 Decay Properties

At leading order in electroweak perturbation theory, the partial width for the decay of the Z^0 boson into a fermion-antifermion pair

$$Z(q) \to f(p)\bar{f}(p') \; , \tag{B.1}$$

is given in the Standard Model by

$$\frac{ig_W}{2\cos\theta_W}\bar{u}(p)\gamma^\mu(V_f - A_f\gamma_5)\upsilon(p')\epsilon_\mu(q). \tag{B.2}$$

The invariant matrix element squared for this process summed (averaged) over final (initial) polarizations is given by

$$\overline{\sum}|\mathcal{M}|^2 = \frac{8}{3}\frac{G_F M_Z^4}{\sqrt{2}}\left(|V_f|^2 + |A_f|^2\right) \; . \tag{B.3}$$

The sum over the three polarizations of the Z^0 boson is performed using

$$\sum_i \epsilon_\mu^{(i)}(q)\epsilon_\nu^{(i)*}(q) = -g_{\mu\nu} + \frac{q_\mu q_\nu}{M_Z^2} \; . \tag{B.4}$$

The two-particle phase space is given by

$$d\Phi_2(P, p_1, p_2) = \frac{1}{8\pi}\frac{2|p_1|}{M_P}\frac{d\Omega}{4\pi} \; , \tag{B.5}$$

where p_1 is the three-momentum of the decay products in the rest frame of the decaying particle, which has mass M_P and $d\Omega$ is the element of solid angle.

The final result for the partial width is

$$\Gamma(Z^0 \to f\bar{f}) = C\frac{G_F M_Z^3}{6\sqrt{2}\pi}\left(|V_f|^2 + |A_f|^2\right) = 332\; C\left(|V_f|^2 + |A_f|^2\right)\; \mathrm{MeV} \tag{B.6}$$

where C is a color normalization factor which is 1 for leptons and 3 for quarks.

Using the result for the partial width of Z^0 we can calculate the branching ratio for the various fermion-antifermion decay modes shown in the table below.

Process	Relative coupling	Branching Ratio
$Z \to \nu_e\bar{\nu}_e, \nu_\mu\bar{\nu}_\mu, \nu_\tau\bar{\nu}_\tau$	$1/2$	$3 \times 6.8\%$
$Z \to e^+e^-, \mu^+\mu^-, \tau^+\tau^-$	$1/4 \ + \ (1/2 - 2\sin^2\theta_w)^2$	$3 \times 3.4\%$

There is also a large branching fraction of the Z^0 boson into neutrinos, which are not detectable. The measurement of the width for decay of the Z^0 boson into invisible particles counts the number of light neutrino species. The theoritical result for the ration of the width into one species of neutrino, divided by the width into one species of lepton is

$$\frac{\Gamma(Z \to \nu\bar{\nu})}{\Gamma(Z \to l\bar{l})} = \frac{2}{1 + (1 - 4\sin^2\theta_W)^2} \approx 1.99 \ . \tag{B.7}$$

Appendix C

The Armenteros-Podolanski Plot

The features of the Armenteros-Podolanski plot can be completely understood by considering the kinematics of the decay of a neutral V^0 candidate into two charged particles ($\Lambda \to p\pi^-$). This system has to be considered in both the laboratory system (in which measurements are made) and in the centre of mass system (in which V^0 is at rest and consequently the two charged particles must come off back-to-back so as to conserve momentum) as shown in figure C.2.

It is clear from figure **??**b that in the centre of mass system the transverse and longitudinal momenta, realitve to the direction in which the V^0 was moving in the laboratory system, are defined

$$q_T^* = p^* \sin\theta^* \tag{C.1}$$

$$q_L^* = p^* \cos\theta^* \tag{C.2}$$

where all quantities in the centre of mass system are denoted by a *.

To express these quantities in the laboratory system requires the use of the Lorentz transformations

$$\begin{pmatrix} E \\ q_L \end{pmatrix} = \begin{pmatrix} \gamma & \gamma\beta \\ \gamma\beta & \gamma \end{pmatrix} \begin{pmatrix} E^* \\ q_L^* \end{pmatrix} \tag{C.3}$$

where $\beta = v/c$: v is the velocity of the particle and c is the speed of light. γ is defined as $\gamma = 1/\sqrt{1-\beta^2}$.

When C.3 is expanded it will give a definition of q_L in terms of q_L^*

$$q_L = \gamma\beta E^* + \gamma q_L^* \tag{C.4}$$

Using the above

$$q_L = \gamma\beta E^* + \gamma p^* \cos\theta^* \tag{C.5}$$

Transverse momentum is Lorentz invariant and so

$$q_T = q_T^* = p^* \sin\theta^* \tag{C.6}$$

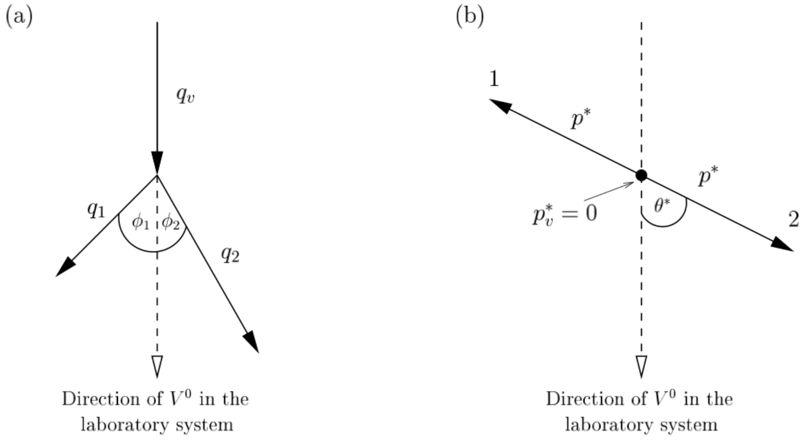

Figure C.1: The decay of a neutral V^0 into two charged tracks in (a) the laboratory system and (b) the centre of mass system. In the latter system the two decay particles must come off back-to-back so as to conserve momentum.

Armenteros α is defined

$$\alpha = \frac{q_L^+ - q_L^-}{q_L^+ + q_L^-} \tag{C.7}$$

Using the C.5 and given that $\cos(\theta + \pi) = -\cos\theta$, the above becomes

$$\alpha = \frac{\gamma\beta(E_1^* - E_2^*) + 2\gamma p^* \cos\theta^*}{\gamma\beta(E_1^* + E_2^*)} \tag{C.8}$$

assuming particle 1 is the positively charged particle and particle 2 is the negatively charged one.

Now energy, E^*, is conserved and so in the centre of mass system,

$$E^* = E_1^* + E_2^* \tag{C.9}$$

where using the relativistic equation $E^2 = p^2 + m^2$, E^*, E_1^* and E_2^* are given by

$$E^* = m_v, \quad E_1^* = \sqrt{p^{*2} + m_1^2}, \quad E_2^* = \sqrt{p^{*2} + m_2^2} \tag{C.10}$$

where in the centre of mass system the momentum of the V^0, p_v^*, is zero.

By substituting C.9 into C.10

$$E_1^* + E_2^* = m_v \tag{C.11}$$

The above can be used in C.8, along with the approximation that relativistically $v \approx c$ and so $\beta \approx 1$. The γs cancel and so C.8 becomed

$$\alpha = \frac{E_1^* - E_2^*}{m_v} + \frac{2p^* \cos\theta^*}{m_v} \tag{C.12}$$

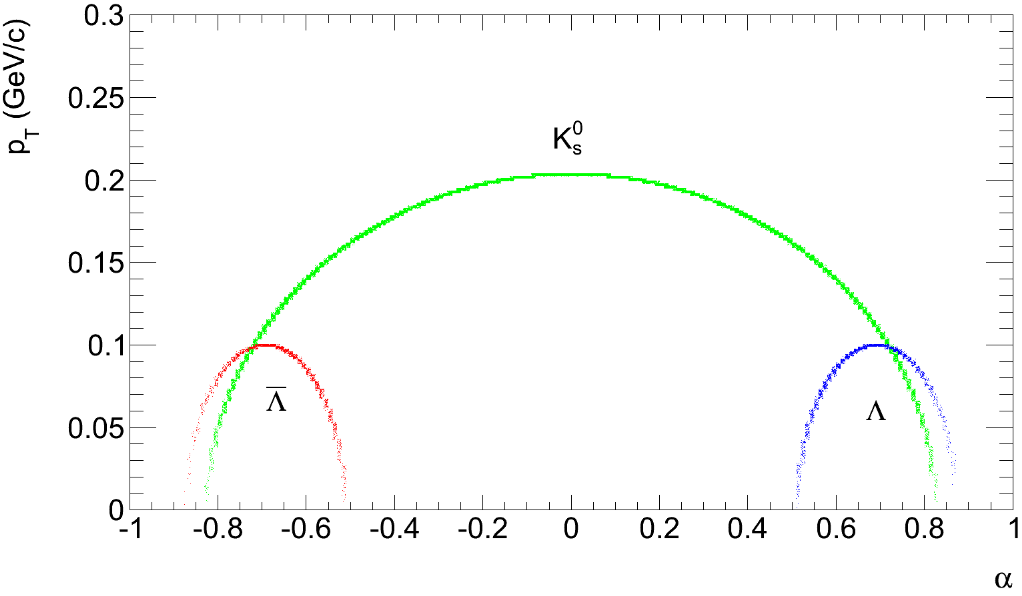

Figure C.2: Theoretical curves for Λ, $\bar{\Lambda}$ and K_s^0 .

From the above the variables $\bar{\alpha}$ and a can be defined

$$\bar{\alpha} = \frac{E_1^* - E_2^*}{m_v} \tag{C.13}$$

$$a = \frac{2p^*}{m_v} \tag{C.14}$$

and so

$$\alpha = \bar{\alpha} + a\cos\theta^* \tag{C.15}$$

Using C.6

$$\left(\frac{\alpha - \bar{\alpha}}{a}\right)^2 + \left(\frac{q_T}{p^*}\right)^2 = 1 \tag{C.16}$$

which is simply the equation of an ellipse.

This page intentionally left blank

Bibliography

[1] R. Hanbury-Brown and R.Q. Twiss, Philos. Mag. 45 (1954) 663.

[2] ATLAS Collaboration:"The ATLAS experiment at the CERN LHC", JINST 3 S08003 (2008).

[3] T. Alexopoulos, Ph.D. thesis, University of Wisconsin, Madison, 1991.

[4] G. Goldhaber et al., Phys. Rev. 120 (1960) 300.

[5] M.Plümmer, L.V. Razumov and R.M. Weiner, Phys. Lett. B 286 (1992) 335.

[6] G. Baym, Lectures on Quantum Mechanics, The Benjamin/Cummings Publishing Company, INC. 1981.

[7] R.C. Femow, Introduction to Experimental Particle Physics, Cambridge University Press, 1986.

[8] ATLAS Collaboration, The ATLAS Experiment at the CERN Large Hadron Collider, JINST 3 (2008) S08003.

[9] ATLAS Collaboration, Determination of the muon reconstruction efficiency in ATLAS at the Z resonance in $p - p$ collisions at $\sqrt{s} = 7$ TeV , ATLAS-CONF-2011-008 (2011).

[10] ATLAS Collaboration, A measurement of the total $W^{\pm}$ and $Z/^{*}$ cross sections in the e and μ decay channels and of their ratios in $p - p$ collisions at $\sqrt{s} = 7$ TeV with the ATLAS detector, ATLAS note: ATLAS-CONF-2011-041.

[11] F. Halzen and A. D. Martin, Quarks and Leptons: An Introductory Course in Modern Particle Physics. Wiley, 1984.

[12] Particle Data Group, K. Nakamura et al., Review of particle physics, J. Phys. G37 (2010) 075021.

[13] R. Ellis, W. Stirling, and B. Webber, QCD and collider physics, vol. 8. 1996.

[14] ATLAS Run Queries, http://atlas-runquery.cern.ch/.

[15] https://twiki.cern.ch/twiki/bin/view/AtlasPublic/ LuminosityPublicResults.

[16] R. Brun and F. Rademakers, ROOT: An object oriented data analysis framework, Nucl. Instrum. Meth. A389 (1997) 81.